

1 A Long-Lived Lunar Magnetic Field Powered by Convection in the Core and a
2 Basal Magma Ocean

3
4 Saira Hamid^{1,2}, Joseph G. O'Rourke², Krista M. Soderlund³

5
6 ABSTRACT

7
8 An internally generated magnetic field once existed on the Moon. This field
9 reached high intensities ($\sim 10\text{--}100\ \mu\text{T}$, perhaps intermittently) from $\sim 4.3\text{--}3.6$
10 Gyr ago and then weakened to $\lesssim 5\ \mu\text{T}$ before dissipating by $\sim 1.9\text{--}0.8$ Gyr ago.
11 While the Moon's metallic core could have generated a magnetic field via a
12 dynamo powered by vigorous convection, models of a core dynamo often fail to
13 explain the observed characteristics of the lunar magnetic field. In
14 particular, the core alone likely may not contain sufficient thermal,
15 chemical, or radiogenic energy to sustain the high-intensity fields for >100
16 Myr. A recent study by Scheinberg et al. suggested that a dynamo hosted in
17 electrically conductive, molten silicates in a basal magma ocean (BMO) may
18 have produced a strong early field. However, that study did not fully explore
19 the BMO's coupled evolution with the core. Here we show that an early BMO
20 dynamo that dovetails with a later core dynamo, primarily driven by inner
21 core growth, can explain the timing and staged decline of the lunar magnetic
22 field. We compute the thermochemical evolution of the lunar core with a 1-D,
23 parameterized model tied to extant simulations of mantle evolution and BMO
24 solidification. Our models are most sensitive to four parameters: the
25 abundances of sulfur and potassium in the core, the core's thermal
26 conductivity, and the present-day heat flow across the core-mantle boundary.
27 Our models best match the Moon's magnetic history if the bulk core contains
28 $\sim 6.5\text{--}8.5\ \text{wt}\%$ sulfur, in agreement with seismic structure models.

¹ Corresponding author sshamid1@asu.edu

² School of Earth and Space Exploration, Arizona State University, Tempe, AZ 85287, USA

³ Institute for Geophysics, Jackson School of Geosciences, University of Texas at Austin, Austin, TX 78758, USA

29 1. INTRODUCTION
30

31 Paleomagnetic analyses of lunar meteorites and Apollo samples suggest that
32 a high-intensity magnetic field of $\sim 10\text{--}100\ \mu\text{T}$ existed $\sim 4.25\text{--}3.56$ billion years
33 (Gyr) ago, followed by a weakened field of $\lesssim 5\ \mu\text{T}$ that persisted until $\sim 1.9\text{--}$
34 0.8 Gyr ago (e.g., Tikoo et al. 2014, Tikoo et al. 2017, Mighani et al. 2020,
35 **Strauss et al. 2021**, Wieczorek et al. 2022). Generation of an intrinsic
36 magnetic field via dynamo action requires vigorous motion of an electrically
37 conducting fluid such as the liquid portion of a metallic core (e.g., Bullard
38 **1949**, Elsasser 1950, Bullen 1954, Glatzmaier and Roberts 1995, Kageyama et
39 **al. 1995**). Various observations indicate that the Moon has a metallic core,
40 including seismic data from the Apollo missions (e.g., Garcia et al. 2011,
41 Weber et al. 2011), electromagnetic sounding (e.g., Hood et al. 1999, Shimizu
42 et al. 2013), and gravity data from the Gravity Recovery and Interior
43 Laboratory (GRAIL) mission (e.g., Williams et al. 2014), which are all
44 consistent with a core radius of $\sim 250\text{--}430$ km. Today, a solid inner core with
45 a radius up to ~ 250 km may also exist (Williams et al. 2014, Weber et al.
46 2011).

47 Models of the thermal evolution of the lunar core have difficulty
48 reproducing the history of the lunar magnetic field (e.g., Evans et al. 2018,
49 Laneuville et al. 2014, Scheinberg et al. 2015). These models have two goals
50 that often seem incompatible: 1) sustaining a long-lived field (e.g.,
51 multiple Gyr) and 2) sustaining an early strong field (i.e., $>10\ \mu\text{T}$, at least
52 for the first ~ 1 Gyr). With available energy sources internal to the core
53 (e.g., radiogenic, latent, and chemical energy, plus inner core precession),
54 the Moon can sustain a low-intensity field for long durations (e.g.,
55 Laneuville et al. 2014; Scheinberg et al. 2015, Evans et al. 2018, Stys &
56 Dumberry 2020). **However, Evans et al. (2018) showed that those energy sources**
57 **could only sustain a $>10\ \mu\text{T}$ field for <50 Myr, assuming that the radius of**
58 **the core is ≤ 380 km as favored by recent studies (Weber et al. 2011, Williams**
59 **et al. 2014).** So, sustaining a $>10\ \mu\text{T}$ field for ~ 1 Gyr is highly improbable
60 without an external mechanism, such as mechanical stirring between the solid
61 mantle and the liquid core from precession of the lunar spin axis (e.g.,
62 Dwyer et al. 2011; Meyer & Wisdom 2010; Čuk et al. 2019) and/or impact-
63 induced changes in the rotation rate of the solid mantle (e.g., Le Bars et
64 al. 2011). Another solution to this seeming paradox is to invoke
65 intermittency during the high-intensity epoch. For example, a recent study
66 proposed that foundering of relatively cold material in the lunar mantle may
67 have excited episodes of rapid core cooling that lasted <1 Myr (Evans & Tikoo

68 2022). Finally, in this study, we explore the idea that the core is not the
69 only potential host for a lunar dynamo as argued by Scheinberg et al. (2018).

70 71 1.1. A Basal Magma Ocean

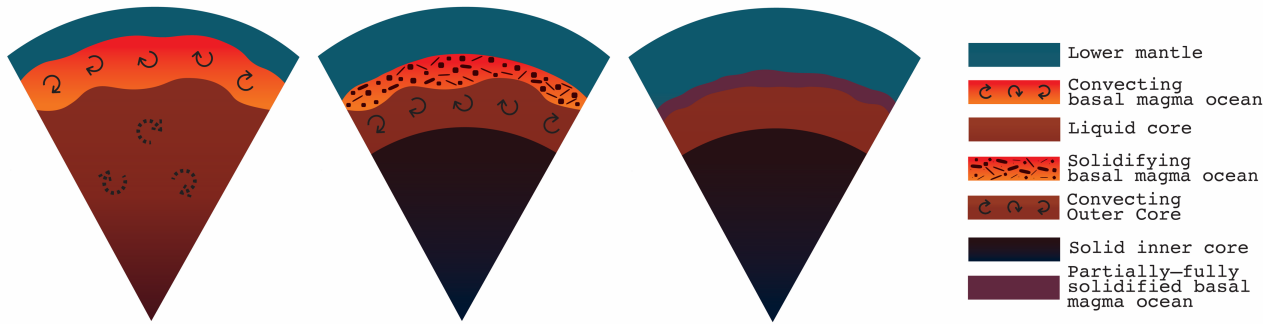
72
73 Almost any scenario for the formation of the Moon involves enough
74 energy to melt much of the newly formed Moon (e.g., Hartmann & Davis 1975,
75 Warren 1985, **Elkins-Tanton et al. 2011, Canup 2012, Čuk & Stewart 2012,**
76 **Nakajima & Stevenson 2014**). The resulting magma ocean is often modeled as
77 solidifying in three primary stages (e.g., Elardo et al. 2011, Wieczorek et
78 al. 2006, Hess & Parmentier 1995, Hamid & O'Rourke 2022). As the lunar magma
79 ocean cooled, dense mafic cumulates (e.g., olivine and pyroxene) formed and
80 sank towards the bottom. Once most of the lunar magma ocean solidified,
81 anorthositic plagioclase with lower density began to crystallize, rising to
82 form the lunar crust. The final, highly evolved liquids, "ur-KREEP" (enriched
83 in uranium, thorium, potassium, rare earth elements, and phosphorus),
84 alongside ilmenite-rich cumulates, would be gravitationally unstable because
85 of their high densities. Some fraction of this ur-KREEP-ilmenite mixture
86 eventually sank to the base of the mantle, ponding as a layer above the core-
87 mantle boundary (CMB). **Radiogenic heat from elements present in this fallen**
88 **ur-KREEP layer, such as uranium, thorium, and potassium (with concentrations**
89 **up to ~12 times higher than the bulk mantle), could fully melt this layer**
90 **(e.g., Scheinberg et al. 2018)**. The result is a basal magma ocean (BMO) that
91 persists until convective heat loss into the overlying mantle causes
92 solidification. The nominal model of Scheinberg et al. (2018) had a 301-km
93 peak thickness BMO; less conservative models had BMO thicknesses up to 450
94 km.

95 Models are equivocal about the lifetime of a BMO. For example, a small
96 compositional density contrast between the BMO and the overlying mantle could
97 make the BMO short-lived (Stegman et al. 2003). In this scenario, thermal
98 expansion of the BMO can overcome the compositional density contrast between
99 the BMO and the overlying mantle, causing the BMO to buoyantly rise and re-
100 mix with the mantle. Conversely, the persistence of interstitial fluid
101 trapped within the solidified cumulates could leave the BMO sequestered at
102 the CMB (Elkins-Tanton et al. 2011, Scheinberg et al. 2018). Indeed,
103 interpretations of geophysical data (Khan et al. 2014), seismic data (Weber
104 et al. 2011), and gravity data (Williams et al. 2014) have indicated that a
105 deep-seated zone of partial melt at the CMB may exist today. This partial
106 melt could be the last remnant of a once-thicker BMO.

107 A BMO can sustain a dynamo if it is vigorously convecting and has
108 sufficiently high electrical conductivity, σ (e.g., Scheinberg et al. 2018,
109 Ziegler & Stegman 2013, Stixrude et al. 2020). Although liquid silicates
110 generally have low electrical conductivity at temperatures and pressures
111 found in the lunar mantle, the lunar BMO may have had a particularly high
112 titanium and iron content (Hess & Parmentier 1995). **While a sufficient**
113 **conductivity may be plausible, a weakness in this hypothesis remains when**
114 **explaining how high titanium and iron contents translate into a more**
115 **conductive BMO. The titanium- and iron-bearing silicates would likely need to**
116 **be in a metallic form for this to occur, which would imply a highly reduced**
117 **magma ocean (e.g., Rzehak et al. 2021, 2022). Fortunately, the BMO dynamo**
118 **hypothesis can be explored regardless of this uncertainty. Assuming the BMO**
119 **is in fact sufficiently conductive (several thousand S/m), the BMO has an**
120 **advantage over the core in terms of generating strong surface fields because**
121 **it is closer to the lunar surface. Magnetic fields attenuate rapidly with**
122 **distance, so a magnetic field generated in the BMO would appear stronger at**
123 **the surface than a magnetic field generated with the same strength in the**
124 **core (e.g., Scheinberg et al. 2018, Stevenson 1983, Christensen 2010).**

125 Our study is built on the whole-Moon models presented in Scheinberg et al.
126 (2018). That study focused on the solid mantle and BMO to explain the **early,**
127 **strong (i.e., >10 μT)** lunar dynamo. **Both the BMO and the core were assumed to**
128 **be well-mixed on the timescales of the overlying solid mantle convection and**
129 **were assumed to have an adiabatic temperature gradient, except during the**
130 **phase in which the magma ocean increases in temperature.** That study further
131 tested the sensitivity of their model to the reference viscosity in the solid
132 mantle, the fraction of the KREEP layer that remained near the surface, and
133 the fraction of radioactive material concentrated in the BMO. At the start of
134 their simulations, the BMO exhibited a rapid increase in heat flow from
135 radiogenic heating, followed by a steady decline to its solidus temperature.
136 A detailed model of the core was not included because the core is relatively
137 small and does not strongly affect the thermal evolution of the BMO and solid
138 mantle. In this study, we do not directly model the BMO-hosted dynamo, but
139 rather focus on the core to test if models of lunar evolution that feature a
140 BMO as a boundary condition can explain both the strong, early dynamo and the
141 later dynamo that produced much weaker fields (Figure 1).

142
143
144
145



146 Figure 1: We study three stages in the coupled evolution of the lunar BMO and
 147 core. (Left) Convection in the BMO produced an early, high intensity dynamo
 148 ~4.25–3.56 Gyr ago while the core was fully liquid. Dashed arrows indicate that
 149 in limited scenarios, thermal convection in the core may have occurred in tandem
 150 with the BMO-hosted dynamo. (Middle) Compositional convection in the core
 151 produced a late, low intensity dynamo until ~1.9–0.8 Gyr ago once the inner
 152 core started growing and the BMO began to solidify. (Right) The internal field
 153 ceased ~1 Gyr ago once the BMO solidified sufficiently, the inner core grew too
 154 large, and convection ceased in the liquid outer core.
 155

156 2. METHODS

157 2.1. Structure of the Metallic Core

158 We assume that the lunar core is an iron alloy that starts fully liquid
 159 with no chemical or thermal stratification. To build our models, we assume
 160 that sulfur is the major light element in the core, given its siderophile
 161 behavior and cosmochemical abundance (e.g., Pommier et al. 2018, Cameron
 162 1973). Our models also include trace amounts of potassium as a source of
 163 radiogenic heating. Other studies have speculated about the possible roles of
 164 other light elements in the lunar core, including carbon (e.g., Dasgupta et
 165 al. 2009), silicon (e.g., Berrada et al. 2020), and phosphorous (e.g., Yin et
 166 al. 2019). However, the complexities of a core with multiple light elements
 167 are beyond the scope of this study.
 168

169 A 1-D, parameterized description of the structure of the core is the
 170 foundation of our models. As described in Appendix A, we used hydrostatic
 171 equilibrium and equations of state detailed in Khan et al. (2017) to
 172 calculate the radial profiles of density, pressure, temperature, and
 173 gravitational acceleration within the core. Our fiducial structural model
 174 assumes that the core contains 6 wt% sulfur and has a central pressure and
 175 temperature of 5.15 GPa and 1800 K, respectively, **to match the core**
 176 **parameters described in Scheinberg et al. (2018)**. The radius of the core is
 177 then 350 km, which is also the same as in Scheinberg et al. (2018) and in
 178 agreement with available observational constraints. However, Scheinberg et
 179 al. (2018) used an average density for the core appropriate to a composition
 180 of pure iron, which would increase the total mass of the core by ~20%.
 181

182 Fortunately, most of the structural parameters that are key to our
183 thermodynamic calculations (e.g., K_0 , K_1 , $L\rho$, and $A\rho$ in Table D1) are not
184 sensitive to the bulk composition of the core. Sulfur is most important to
185 the thermal evolution of the lunar core via its effect on the bulk liquidus.
186 Using a fixed sulfur content to calculate other parameters (e.g., ρ_0 , P_0 , and
187 M_c) should only introduce inaccuracies that are smaller than the observational
188 uncertainties.

189

190

2.2. Energetics of the Metallic Core

191

192

193

194

195

196

197

198

199

200

201

202

203

204

205

206

207

$$Q_{CMB} = Q_L + Q_G + Q_R + Q_S \quad (1)$$

208

209

210

211

212

213

214

215

216

217

218

219

The overlying BMO controls the evolution of the core. From the results of Scheinberg et al. (2018), we know the total heat flow across the core-mantle boundary (Q_{CMB}) over time until the BMO solidifies. Assuming that the entire core is well mixed and at a temperature equal to the temperature of the BMO, our models begin when the BMO starts cooling down. After the BMO is fully solid, our models assume that Q_{CMB} changes linearly to a value that we specify for the present day, which could be the same or (much) less than the value of Q_{CMB} when the BMO solidifies. Those models begin at 4.2 Gyr ago and predict that the BMO heats up for the first ~200 Myr or so. **For simplicity, we assume that the core is heated uniformly, although it is not isothermal, during this brief period before the entire deep interior starts cooling.** With the boundary condition provided by the BMO model, we then use a well-established method, developed to study Earth's core (e.g., Labrosse 2015), to model the thermodynamic evolution of the lunar core once it starts cooling again. First, we can calculate the global heat budget of the core:

Here, Q_S represents the secular cooling of the core and is proportional to the core's specific heat. We assume that trace amounts of potassium produce radiogenic heating (Q_R). The remaining two terms are only relevant once the inner core nucleates: energy from latent heat (Q_L) and gravitational energy from the exclusion of light elements into the outer core (Q_G) that are released as the inner core grows.

Given the total heat flow, we solve for the rate of change in the CMB temperature. As shown in Appendix B, most of the terms on the right side of equation (1) are products of dT_{CMB}/dt and a term (\tilde{Q}) that depends only on the thermodynamic properties of the core and its structural parameters. Each of those terms is calculable using polynomial functions. We can thus rearrange equation (1):

220

$$\frac{dT_{CMB}}{dt} = \frac{Q_{CMB} - Q_R}{\overline{Q_S} + \overline{Q_G} + \overline{Q_L}} \quad (2)$$

221

222

223

224

225

226

227

228

229

230

231

232

233

The growth rate of the inner core is directly proportional to dT_{CMB}/dt also (see Appendix B). Because equation (1) does not include any secular cooling of the inner core, we are implicitly assuming that the inner core is perfectly insulating (i.e., with zero thermal conductivity). We could also model a conductive inner core with infinite thermal conductivity, but the associated heat flow is a minor contribution to the global heat budget if the inner core extends to only <75% of the core radius, as expected at present day. Technically, equations (1) and (2) are only valid if the liquid portion of the core is convective and thus maintaining a nearly adiabatic thermal profile. This assumption is not valid at present day and thermal stratification probably exists **since the core heat flux was likely lower than the heat flux that can be conducted along the adiabat for most of the Moon's evolution (e.g., Laneuville et al. 2014).**

234

235

236

237

238

239

240

241

242

243

244

Our models must use a liquidus for the core that depends on the bulk composition. **We adapted Equation 29 from Buono & Walker (2011), in which the Fe-FeS liquidus is fit to a polynomial that is fourth-order in both pressure and sulfur content. Our model uses an approximation of the liquidus that is first-order in both pressure and sulfur content. Specifically, we estimated the approximate pressure derivative (dT_L/dP) based on the difference in the liquidus temperatures at 5.15 GPa at the center of the core versus 4.43 GPa at the CMB for 6 wt% sulfur. We found the approximate compositional derivative (dT_L/dc) based on the difference in liquidus temperatures for 0 vs. 25 wt% sulfur at 5 GPa (Table D1).**

245

2.3. Strength of a Core-Hosted Dynamo

246

247

248

249

250

251

252

253

254

255

256

257

Vigorous convection in the core can produce a dynamo through the conversion of kinetic to magnetic energy. In general, there are two types of power sources for convection in the core. First, the buoyancy of light elements released from inner core solidification can drive compositional convection. Second, thermal buoyancy from secular cooling of the core, freezing of the inner core, and/or radiogenic heating can power thermal convection. For thermal convection to occur from secular cooling alone, Q_{CMB} must exceed the adiabatic heat flow (Q_{AD}), which equals the product of the thermal conductivity of the core and the adiabatic temperature gradient (see Appendix B). Once the inner core nucleates, the critical heat flow above which convection occurs is lowered.

258 We combined the energy and entropy budgets for the core to calculate the
 259 total dissipation available to power a dynamo (e.g., Labrosse 2015):

$$260 \quad \Phi_{CMB} = \Phi_L + \Phi_G + \Phi_R + \Phi_S - \Phi_K. (3)$$

261 Here, Φ_L , Φ_G , Φ_R , and Φ_S are the dissipation terms associated with Q_L , Q_G , Q_R ,
 262 and Q_S , respectively. The last term (Φ_K) corresponds to the entropy sink
 263 associated with thermal conduction in the core. Appendix B contains the
 264 polynomial expressions for each dissipation term, which, like the energy
 265 terms, depend on the thermophysical properties of the core and its overall
 266 cooling rate. Critically, we assume a dynamo exists if the dissipation is
 267 positive (i.e., if $\Phi_{CMB} > 0$ W). **This criterion yields similar predictions as**
 268 **another often-used criterion, which is that the magnetic Reynolds number**
 269 **(defined below) exceeds a critical value of 50–100 (e.g., Roberts 2007).**

270 Several scaling laws are available to convert the dissipation (in Watts)
 271 into the strength of the magnetic field at the equatorial surface of the Moon
 272 (in Teslas). First, we use a scaling law based on core energetics (see
 273 Appendix B) to calculate the total dipole moment (D_M) of the Moon (units of A
 274 m²). **In this case, assuming the lunar magnetic field is dipolar, the surface**
 275 **field strength at the magnetic equator is**

$$276 \quad B = \frac{\mu_0 D_M}{4\pi R_M^3}, (4)$$

277 where R_M is the radius of the Moon and μ_0 is the permeability of free space.
 278 Additionally, we estimate the magnetic field intensity using three scaling
 279 laws that relate the associated convective power to the anticipated
 280 convective velocities (e.g., Christensen 2010). These scaling laws use
 281 different force balances to calculate the strength of the magnetic field in
 282 the core (B_C). First, mixing length theory (ML) assumes a balance between
 283 inertial and buoyancy forces:

$$284 \quad B_{ML} = \left[2c\mu_0(\rho_0 R_C^2 \Phi_{CMB}^2)^{\frac{1}{3}} \right]^{\frac{1}{2}}, (5)$$

285 where $c \sim 0.63$ is a constant of proportionality, ρ_0 is the central density in
 286 the core, and R_C is the radius of the core. Second, assuming a balance of
 287 Coriolis, inertial, and gravitational (Archimedes) (CIA) forces yields:

$$288 \quad B_{CIA} = \left[2c\mu_0(\rho_0^2 R_C^4 \Omega \Phi_{CMB}^3)^{\frac{1}{5}} \right]^{\frac{1}{2}}, (6)$$

289 where Ω is the present-day angular velocity of the Moon, which may
 290 underestimate the field strength since the Moon likely rotated faster in the
 291 past. Third, the Magneto-Archimedes-Coriolis (MAC) scaling assumes a balance
 292 between Lorentz, gravitational, and Coriolis forces:

293

$$B_{MAC} = \left[2c\mu_0(\rho_0 R_C^2 \Omega \Phi_{CMB})^2 \right]^{\frac{1}{2}}. (7)$$

294

With these three scaling laws, we calculate the surface field strength of the dipole component as

295

296

$$B_S = \frac{1}{7} B_C \left(\frac{R_C}{R_M} \right)^3. (8)$$

297

298

299

300

301

302

303

304

305

306

307

308

309

2.4. Local Rossby Number

310

311

312

313

314

We further assess the dipolarity of the Moon's magnetic field, particularly whether a dipole-dominated or multipolar dynamo may be preferred. Although there are numerous hypotheses for what controls the breakdown of the dipole (e.g., Soderlund & Stanley 2020), we consider here the local Rossby number:

315

$$Ro_l = \frac{U}{2\Omega l}, (9)$$

316

317

318

319

320

321

322

323

324

325

326

327

where $\Omega = 2\pi/T$ is the angular velocity of the Moon, T is the rotation period in seconds, l is the characteristic length scale of the flow, and U is the characteristic fluid velocity. This dimensionless parameter measures the relative importance of inertial to Coriolis forces at convective length scales. Numerical models of **planetary dynamos** indicate that dipole-dominated solutions tend to be found approximately when $Ro_l < 0.1$ (i.e., when inertial effects are relatively weak compared to rotation), with multipolar solutions occurring for larger Ro_l values (e.g., Christensen & Aubert 2006).

In order to estimate this parameter, we assume a characteristic fluid velocity and length scale following scaling law predictions as done for the magnetic field strengths (e.g., Christensen 2010). The mixing length (ML) scaling yields

328
$$U_{ML} = \left(\frac{\Phi_{CMB} R_C}{\rho_0} \right)^{\frac{1}{3}}, \quad l_{ML} = R_C, \quad RO_{L,ML} = \left(\frac{\Phi_{CMB} R_C}{\rho_0} \right)^{\frac{1}{3}} (2 \Omega R_C)^{-1}, \quad (10)$$

329 the Coriolis, inertial, and gravitational (Archimedes) (CIA) scaling yields

330
$$U_{CIA} = \left(\frac{\Phi_{CMB}}{\rho_0} \right)^{\frac{2}{5}} \left(\frac{R_C}{\Omega} \right)^{\frac{1}{5}}, \quad l_{CIA} = \left(\frac{U_{CIA} R_C}{\Omega} \right)^{\frac{1}{2}}, \quad RO_{L,CIA} = \left(\frac{\Phi_{CMB}}{\rho_0} \right)^{\frac{2}{5}} \left(\frac{R_C}{\Omega} \right)^{\frac{1}{5}} (4 \Omega U_{CIA} R_C)^{-\frac{1}{2}}, \quad (11)$$

331 and the Magneto-Archimedes-Coriolis (MAC) scaling yields

332
$$U_{MAC} = \left(\frac{\Phi_{CMB}}{\rho_0 \Omega} \right)^{\frac{1}{2}}, \quad l_{MAC} = R_C, \quad RO_{L,MAC} = \left(\frac{\Phi_{CMB}}{\rho_0 \Omega} \right)^{\frac{1}{2}} (2 \Omega R_C)^{-1}. \quad (12)$$

333 Here, $\phi = \Phi_{CMB} / V_{oc}$ is the volumetric thermodynamically available power over
 334 the fluid core. **We could also use these velocity scalings to confirm that the**
 335 **magnetic Reynolds number, which relates the Ohmic diffusion timescale to the**
 336 **convective timescale, exceeds the critical value of -50 for magnetic field**
 337 **generation to occur (e.g., Roberts 2007). With the definition**

338
$$Re_m = \mu_0 \sigma U l, \quad (13)$$

339 **a flow velocity faster than -0.1–1 mm/s produces $Re_m > 50$ if we assume the**
 340 **length scale is equal to the core radius and the electrical conductivity is σ**
 341 **- 10^5 to 10^6 S m $^{-1}$ (e.g., Berrada et al. 2020, Pommier et al. 2020).**

342

343

2.5. Model Parameters

344

345 Our model ingests the BMO model outputs from Scheinberg et al. (2018) and
 346 calculates the energy and dissipation budgets for the core to determine when
 347 the core may host a dynamo (see Table D2). Following the nomenclature of
 348 Scheinberg et al. (2018), **naming of the BMO models corresponds to the**
 349 **parameters chosen to describe the mantle and the initial solidification of**
 350 **its magma ocean. For example, 'V19' indicates a reference mantle viscosity of**
 351 **10^{19} Pa s, 'K50' indicates that 50% of the KREEP layer remained trapped near**
 352 **the surface, and 'p54' indicates that 54% of the internal radiogenic heating**
 353 **occurs in the sunken KREEP material.** We focus on the BMO models that generate
 354 magnetic fields with lifetimes of <2.9 Gyr for consistency with the
 355 paleomagnetic record (e.g., Mighani et al. 2020). We adopt the nominal BMO
 356 case, V19K50p54, as the basis for our nominal model of the core as it assumes
 357 moderate yet reasonable values for the mantle parameters. To test the
 358 sensitivity of our models to the properties of the core, we scan across four
 359 different parameters: the abundance of sulfur and potassium in the core, the
 360 thermal conductivity of the core, and the present-day heat flux at the CMB.

361 As with other planets, the Moon's core is expected to be an alloy of iron
 362 and light elements, such as sulfur (e.g., Steenstra et al. 2016). Properties

363 of the FeS system are relatively well known (e.g., Fei et al. 1997, 2000,
364 Chudinovskikh & Boehler 2007, Morard et al. 2007, 2008, Stewart et al. 2007,
365 Chen et al. 2008, Buono & Walker 2011, Pommier 2018) and concentrations of
366 sulfur in the lunar core are likely <6–8 wt% based on interpretations of
367 seismic data (e.g., Weber et al. 2011) and models of the lunar core (e.g.,
368 Scheinberg et al. 2015, Laneuville et al. 2014). We vary the sulfur
369 abundance, [S], in the bulk core from 1–9 wt% in increments of 0.5 wt%.

370 Potassium is a potential heat source in planetary cores and soluble in
371 iron alloys at planetary conditions (Murthy et al. 2003, Lee et al., 2004).
372 However, the potassium content of the lunar core remains uncertain. Based on
373 previous studies (e.g., Laneuville et al. 2014, Scheinberg et al. 2015), we
374 test a lower limit of 0 ppm, which assumes a complete lack of radiogenic
375 heating in the lunar core. **Although the lower pressures and temperatures in**
376 **the lunar interior might lead to lower amounts of potassium in the lunar core**
377 **(e.g., Steenstra et al. 2018), we use plausible concentrations of potassium**
378 **in Earth’s core as an upper limit (e.g., Hirose et al. 2013).** In our models,
379 we assume that potassium is incompatible in the inner core, meaning that the
380 outer core becomes enriched in potassium as the inner core grows. We vary the
381 bulk potassium abundance, [K], from 0–50 ppm in increments of 25 ppm.

382 The thermal conductivity, k_c , of iron alloys defines the adiabatic heat
383 flux of the core. We assume that the maximum plausible value of k_c is $\sim 50 \text{ W m}^{-1}$
384 K^{-1} , cited from thermal conductivity experiments on Fe-FeS alloys in the lunar
385 pressure and temperature range (e.g., Pommier 2018). Small amounts of
386 impurities, such as sulfur, can cause a large reduction in the thermal
387 conductivity. We investigate k_c and [S] independently in our models to isolate
388 the effects of each parameter, but they are coupled in reality. A minimum
389 value of $10 \text{ W m}^{-1} \text{ K}^{-1}$ is selected to represent relatively large impurities of
390 sulfur (e.g., Pommier 2018). Other proposed compositions for the lunar core,
391 such as Fe-Si alloys, have thermal conductivities that are intermediate
392 between these upper and lower bounds (Berrada et al. 2020). Overall, we vary
393 k_c from $10\text{--}50 \text{ W m}^{-1} \text{ K}^{-1}$ in increments of $10 \text{ W m}^{-1} \text{ K}^{-1}$.

394 The present-day heat flux at the CMB is highly uncertain and may have
395 been susceptible to higher heat fluxes out of the lower mantle from the
396 enrichment of water and other incompatible elements during solidification of
397 the lunar magma ocean (e.g., Elkins-Tanton & Grove 2011, Khan et al. 2014,
398 Evans et al. 2014, Weiss & Tikoo 2014, Dygert et al. 2017, Greenwood et al.
399 2018). To monitor how the core’s temperature evolves given a certain heat
400 flow, we test a range of values using thermal evolution models as a guide
401 (e.g., Laneuville et al. 2014). After the BMO solidifies, we assume that Q_{CMB}

402 decreases linearly from the final BMO simulation output ($\sim 0.90\text{--}3.70$ GW) to a
403 heat flux value specified at present. We therefore vary the present-day heat
404 flow, Q_c , from 0–2 GW in increments of 1 GW. **While the lower limit of 0 GW may**
405 **represent an extreme scenario, we want to explore a full range of modeling**
406 **possibilities to account for multiple scenarios for the lunar solid mantle.**
407 **Furthermore, 1-D models for small planetary bodies typically indicate that**
408 **the heat flux varies slightly during most of the core’s evolution (e.g.,**
409 **Laneuville et al. 2014).** We find that model outputs from simulations with a
410 Q_{CMB} equal to the final BMO simulation output are similar to those from models
411 where the Q_{CMB} slightly decreases.

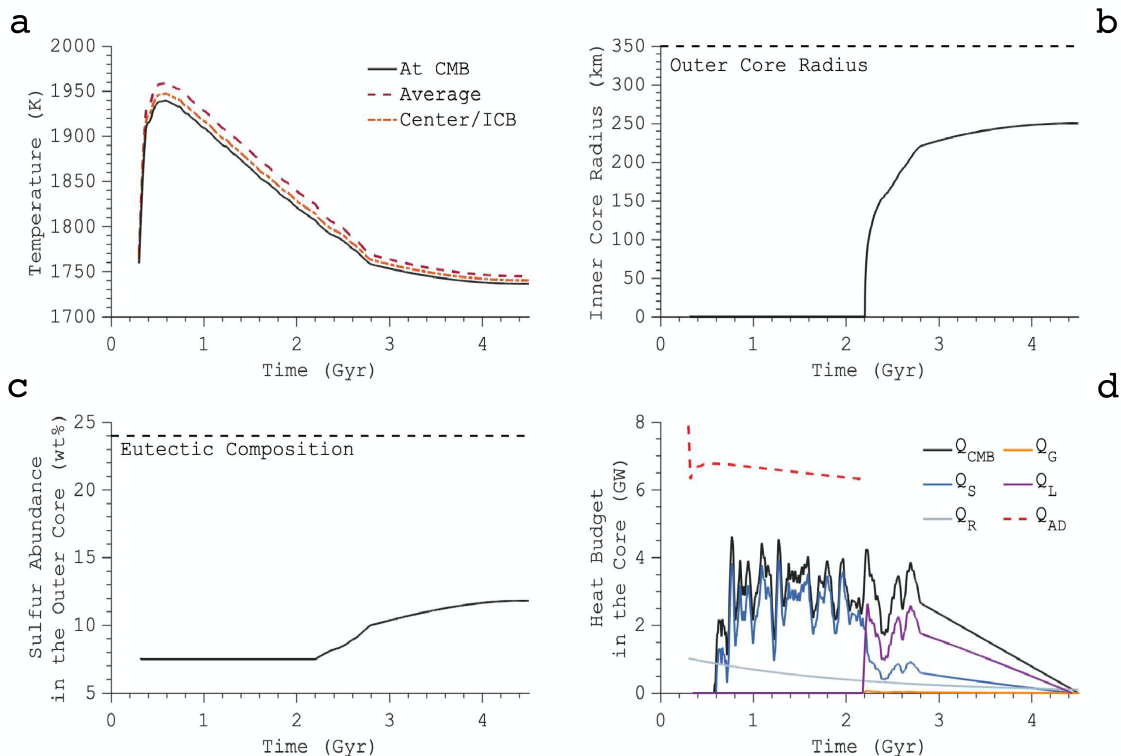
412 Astute readers will realize that our modeling approach makes the
413 cooling rate of the core seem artificially smooth over time after the BMO
414 solidifies. While the BMO exists, we use Q_{CMB} from the 3-D solid mantle models
415 of Scheinberg et al. (2018), which contain realistic time-variability and
416 fluctuations. Once the BMO has presumably solidified, our parameterized model
417 is effectively 1-D and uses a simplified approach for Q_{CMB} to capture the
418 average field strength and lifetime of the core dynamo. In reality, some
419 smaller-scale temporal variations in Q_{CMB} should be expected **and the very last**
420 **time step is not necessarily representative of the end of the time series.**

421 We ran a total of ~ 800 simulations to test the sensitivity of the core
422 model to $[S]$, $[K]$, k_c , and Q_c using BMO model outputs from Scheinberg et al.
423 (2018) as boundary conditions.

424
425
426

3. RESULTS

3.1. Our Nominal Model for the Evolution of the Core

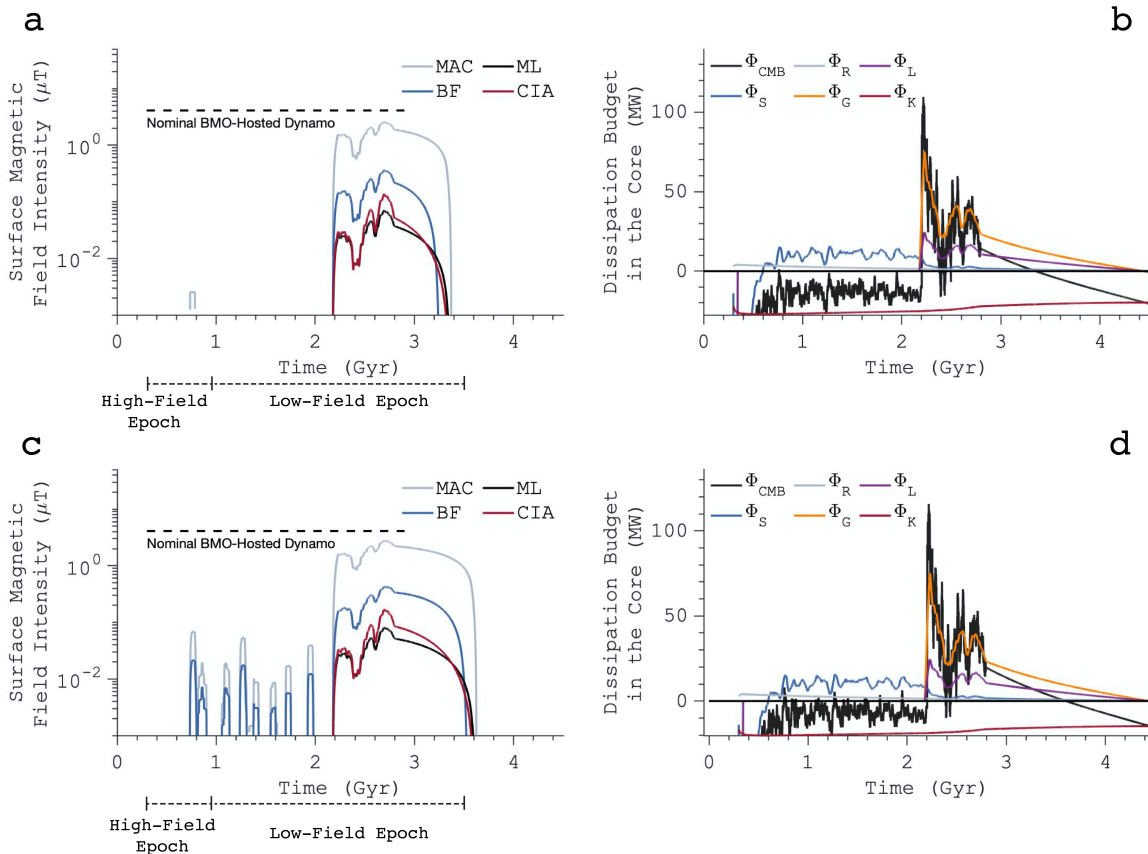


428 Figure 2: Results of the nominal core model with $k_c=40 \text{ W m}^{-1} \text{ K}^{-1}$, $Q_c = 0 \text{ GW}$,
 429 $[S]=7.5 \text{ wt}\%$, and $[K] = 25 \text{ ppm}$ coupled to the nominal BMO model
 430 (V19K50p54). All models began at 4.2 billion years before the present day.
 431 (a) Temperature at the core-mantle boundary (CMB), at the center of the
 432 core or near the inner core boundary (ICB), and the average temperature of
 433 the core. (b) Inner core radius with respect to time. (c) Sulfur abundance
 434 in the outer core with respect to time. (d) Heat budget given by latent
 435 heat, Q_L , radiogenic heating, Q_R , gravitational energy Q_G , adiabatic heat
 436 flow in the core, Q_{AD} , heat flow across the core-mantle boundary, Q_{CMB} , and
 437 secular cooling, Q_S .
 438

439 Our nominal values for the core parameters are $[S] = 7.5 \text{ wt}\%$, $[K] = 25$
 440 ppm, $k_c = 40 \text{ W m}^{-1} \text{ K}^{-1}$, and $Q_c = 0 \text{ GW}$ for the V19K50p54 BMO boundary condition
 441 (Table 1). Figure 2 details the outputs of our nominal model for the core
 442 coupled to the nominal BMO model (i.e., V19K50p54). The temperature at the
 443 CMB begins at $\sim 1760 \text{ K}$ and quickly spikes to $\sim 1940 \text{ K}$ due to radiogenic heating
 444 in the BMO (Fig. 2a). The BMO then begins solidifying as radiogenic heating
 445 declines over time, followed by the core cooling in tandem with the BMO. Once
 446 the BMO solidifies, an inner core forms at $\sim 2.2 \text{ Gyr}$ as relatively pure iron
 447 crystallizes from the inside out (Fig. 2b), expelling sulfur into the outer
 448 core (Fig. 2c). The liquidus temperature of the outer core is lowered as it
 449 is progressively enriched in sulfur. The result is a molten outer core and a
 450 growing inner core. The heat flow is always less than that transported by

451 thermal conduction along the core adiabat, Q_{AD} . After the inner core
 452 nucleates, most extracted heat from the core arises from the release of Q_G and
 453 Q_L (Fig. 2d). **The release of Q_G is nonzero, but small compared to Q_L .** Following
 454 the release of Q_G and Q_L , there is a reduction in the core cooling rate due to
 455 these heat sources acting as a buffer to secular cooling. **We note that the Q_{CMB}**
 456 **is much lower than the heat flow across the upper boundary of the BMO ($Q_B =$**
 457 **~ 100 GW at 2.6 Ga) in Scheinberg et al. (2018) because Q_B includes radiogenic**
 458 **heating in the BMO and also the heat associated with solidifying the BMO.**

459 **Abundant sulfur influences the core's ability to drive a magnetic field**
 460 **by lowering its solidus temperature and controlling the onset of inner core**
 461 **crystallization (discussed further in section 3.2.1). The nominal model**
 462 **produces an inner core radius of 250 km at present day (Fig. 2b) and is**
 463 **consistent with core radii derived from calculated models of lunar gravity**
 464 **data (Williams et al. 2014) and reanalyzed Apollo seismic data (Weber et al.**
 465 **2011).**



466 Figure 3: a) Surface field intensities of the nominal core model where core
 467 convection is driven by inner core growth relatively late in the Moon's
 468 history. The buoyancy flux (BF), mixing length (ML), Coriolis, inertial,
 469 gravitational (Archimedes) (CIA), and Magneto-Archimedes-Coriolis (MAC)
 470 scaling laws are used to estimate surface field intensities of the dipole
 471 component. Surface field intensities are compared to the nominal BMO magnetic

472 field intensity assuming the ML scaling law. (b) The dissipation budget of
473 the nominal core model includes the entropy sink associated with thermal
474 conductivity, Φ_K , the dissipation associated with secular cooling, Φ_S , latent
475 heat, Φ_L , gravitational energy, Φ_G , radiogenic heating, Φ_R , and the
476 dissipation available for a dynamo, Φ_{CMB} . (c) If k_C is lowered to $30 \text{ W m}^{-1} \text{ K}^{-1}$,
477 purely thermal convection occurs intermittently between ~ 0.7 and 2 Gyr. Those
478 resultant surface fields are several times weaker than the BMO-hosted field.
479 (d) Dissipation budget associated with a lower k_C of $30 \text{ W m}^{-1} \text{ K}^{-1}$.
480

481 The lunar BMO suppresses convection in the core by lowering its cooling
482 rate. The core produces a dynamo that begins near the cessation of the
483 nominal BMO-hosted dynamo and ends ~ 1 Ga, **consistent with the lower estimate**
484 **on the cessation of the lunar dynamo** derived from radiometric dating of
485 Apollo 15 samples (e.g., Mighani et al. 2020) (Fig. 3a). The relatively weak
486 surface magnetic field strength of $\lesssim 2.55 \mu\text{T}$ is also consistent with
487 paleomagnetic data and intensities from previous models of the lunar core
488 dynamo (e.g., Laneuville et al. 2014, Tikoo et al. 2014, Tikoo et al. 2017,
489 Evans et al. 2018, Mighani et al. 2020).

490 We next consider different BMO conditions for our core model. **Table 1**
491 **presents the nominal core input parameters for each BMO boundary condition**
492 **used in this study. BMOs with a smaller fraction of KREEP that remained near**
493 **the surface (i.e., V19K25p54 and V18K00p100 in Table 1) have greater initial**
494 **thicknesses and tend to require lower sulfur abundances (6.5–7 wt%) in the**
495 **bulk core to initiate dynamo action during the observed timing of the low-**
496 **intensity epoch. Because a BMO with a greater thickness will have a longer**
497 **lifetime (e.g., Scheinberg et al. 2018), the core will begin crystallizing at**
498 **a later time when the BMO eventually solidifies.** Conversely, models with
499 shallower BMOs (i.e., 301 km) mostly require higher sulfur abundances in the
500 core (7–8.5 wt%) to achieve a core dynamo during the same period. BMO
501 boundary conditions with greater lifetimes additionally suppress inner core
502 growth for longer periods, resulting in smaller inner core radii at present
503 day. **Furthermore, models that contain shallower BMOs match the estimated**
504 **timing of the lunar dynamo if balanced by less radiogenic heating in the core**
505 **(i.e., ≤ 25 ppm of potassium). In general, BMO boundary conditions typically**
506 **require the core to have a higher thermal conductivity (i.e., $\geq 30 \text{ W m}^{-1} \text{ K}^{-1}$)**
507 **to match the estimated timing of the lunar dynamo.**
508

Nominal Core Model Inputs

BMO Boundary Condition	V19K50p54	V19K50p36	V19K50p27	V19K25p54	V18.5K50p54	V18K00p100
BMO lifetime ¹ (Gyr)	2.6	2.0	1.6	2.9	1.2	2.1
BMO thickness ¹ (km)	301	301	301	383	301	450
[S] (wt%)	7.5	7.0	8.5	7.0	8.5	6.5
[K] (ppm)	25	0	0	50	0	50
Q_c (GW)	0	0	0	0	0	0
k_c (W m ⁻¹ K ⁻¹)	40	10	30	40	30	30

Table 1: Nominal core parameters for each BMO boundary condition used in this study.

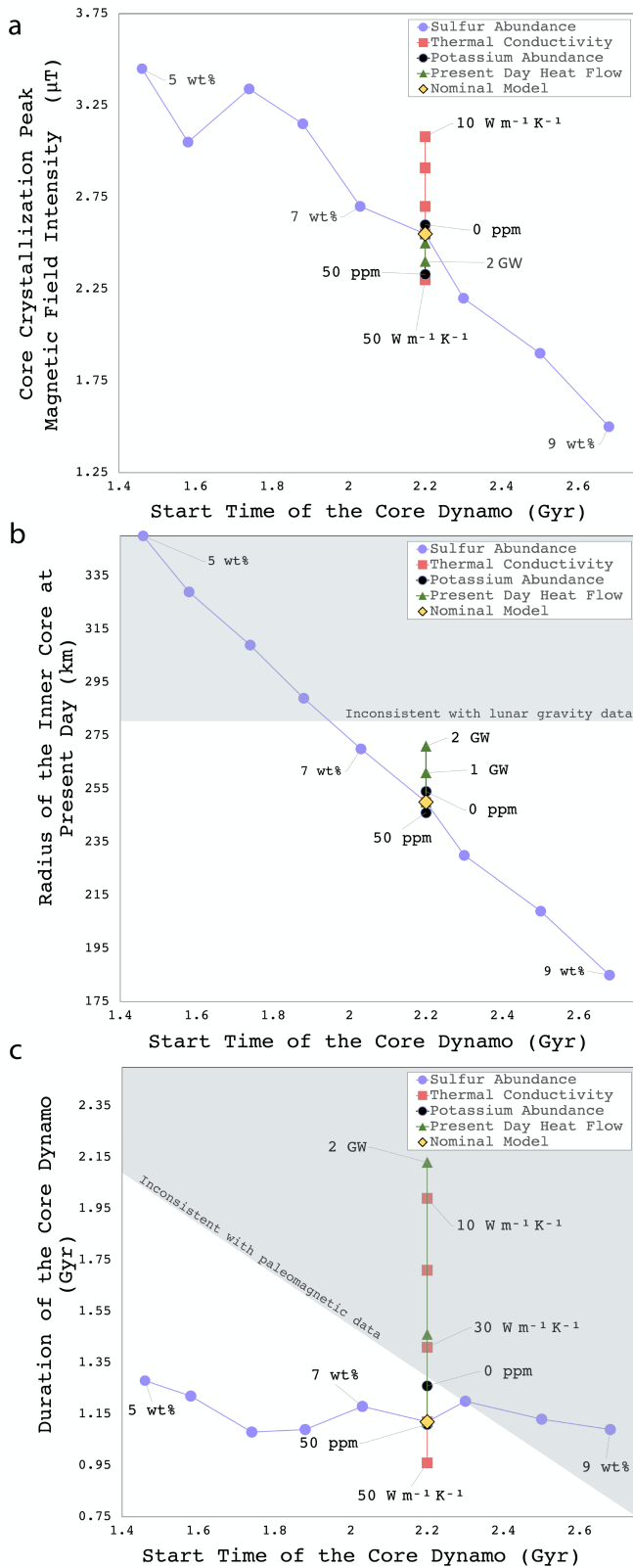
¹Values from Scheinberg et al. (2018), Table 1.

509
510
511

Nominal Core Model Outputs

BMO Boundary Condition	V19K50p54	V19K50p36	V19K50p27	V19K25p54	V18.5K50p54	V18K00p100
Present-day inner core radius (km)	250	257	231	226	262	241
Compositional convection B_{\max} (μT)	0.07 (ML),	0.16,	0.05,	0.03,	0.07,	0.04,
	0.13 (CIA),	0.45,	0.09,	0.04,	0.13,	0.08,
	0.36 (BF),	0.77,	0.27,	0.20,	0.40,	0.28,
	2.55 (MAC)	4.0	2.27	1.7	2.6	2.0
Thermal convection B_{\max} (μT)	- (BF),	0.08,	0.07,	0.02,	0.06,	0.06,
	0.003 (MAC)	0.30	0.31	0.08	0.23	0.28
Combined B_{\max} (μT)	0.07 (ML),	0.16,	0.05,	0.03,	0.07,	0.04,
	0.13 (CIA),	0.45,	0.09,	0.04,	0.13,	0.08,
	0.36 (BF),	0.85,	0.34,	0.22,	0.46,	0.34,
	2.55 (MAC)	4.3	2.58	1.78	2.83	2.28
Peak Local Rossby Number	0.02 (CIA),	0.03,	0.02,	0.02,	0.02,	0.03,
	0.003 (ML),	0.004,	0.003,	0.003,	0.003,	0.003,
	3×10^{-4} (MAC)	4×10^{-4}	2×10^{-4}	2×10^{-4}	2×10^{-4}	3×10^{-4}
Compositional convection duration (Gyr)	1.06 (BF)	1.75	1.78	0.58	2.22	1.34
	1.14 (ML)	1.83	1.90	0.66	2.23	1.42
	1.14 (CIA)	1.75	1.86	0.66	2.23	1.42
	1.12 (MAC)	1.89	1.95	0.71	2.33	1.49
Thermal convection duration (Gyr)	- (ML)	-	0.08	-	-	0.95
	- (BF)	0.87	0.08	0.12	0.85	1.65
	0.05 (MAC)	0.87	0.08	0.12	0.85	1.65
Lifetime of core-hosted dynamo (Gyr)	1.06 (BF)	2.62	1.86	0.7	3.07	2.99
	1.14 (ML)	1.83	1.98	0.66	2.23	2.37
	1.14 (CIA)	1.75	1.86	0.66	2.23	1.42
	1.17 (MAC)	2.76	2.03	0.83	3.18	3.14

Table 2: Compositional and thermal convection in the core sustains low intensity magnetic fields following the cessation of a BMO-hosted dynamo. B_{\max} is the peak magnetic field intensity at the surface according to the ML, CIA, BF, and MAC magnetic field scaling laws, respectively, assuming that the mantle is electrically insulating. Thermal convection B_{\max} corresponds to the BF and MAC scalings, respectively, as the CIA and ML scaling laws predict null fields. The combined B_{\max} is the sum of surface fields generation from thermal and compositional convection. The peak local Rossby number corresponds to the CIA, ML, and MAC scaling laws, respectively. The thermal convection duration corresponds to the ML, BF, and MAC scalings, respectively, as the CIA scaling law predicts null fields.



3.2. Sensitivity Tests

Figure 4: The sensitivities of the nominal core model to core parameters k_c , $[K]$, $[S]$, and Q_c for the nominal V19K50p54 BMO model. (a) The surface magnetic field intensity is most sensitive to k_c and $[S]$ and less sensitive to $[K]$ and Q_c . (b) Our choice of $[S]$ controls the predicted timing of inner core growth and thus, a compositionally-driven core dynamo. The shaded region represents inner core radii that are probably inconsistent with lunar gravity data (e.g., Williams et al. 2014). (c) The duration of the dynamo is predicted to increase with increasing Q_c and decreasing k_c . High $[S]$ tends to delay the onset of inner core crystallization and result in a shorter field duration. The shaded region represents durations that are likely inconsistent with constraints on the end of the lunar dynamo (e.g., Mighani et al. 2020). The magnetic field intensity and the duration of the core dynamo are given by the MAC scaling law.

3.2.1. Influence of Sulfur in the Core

An inverse relationship exists between the sulfur content and the solidus temperature of the core. As the sulfur content increases, the solidus temperature of the Fe-S system decreases, delaying core solidification until lower

561 **temperatures are reached.** Therefore, the timing of inner core growth, and
 562 thus, the start time of compositional convection in our models depends on the

563 sulfur content of the bulk core (Fig. 4a). The **sulfur concentration is viable**
564 **when the end of the core-hosted dynamo matches the lower estimate on the**
565 **cessation of the lunar dynamo at ~1 Gyr (e.g., Mighani et al. 2020).** Initial
566 sulfur abundances of 1–6.5 wt% result in inner core nucleation at higher
567 temperatures, causing the core to solidify rapidly early in its history (Fig.
568 4b). Sulfur abundances from 7–8.5 wt% result in the inner core nucleating
569 near the cessation of the BMO-hosted dynamo. **Increasing the bulk sulfur**
570 **content to >8.5 wt% further delays inner core growth and generally results in**
571 **temporal gaps between the BMO-hosted and core-hosted dynamo,** a complete lack
572 of core dynamo action, or contradictions with timing estimates derived from
573 paleomagnetic data (Fig. 4c). However, if the BMO model assumes a lower solid
574 mantle viscosity (i.e., $V_{18.5K50p54}$), then convective heat transfer is more
575 efficient and results in shorter BMO lifetimes (Scheinberg et al. 2018). As a
576 result, the inner core begins crystallizing earlier and a bulk sulfur content
577 of up to 12 wt% can produce results consistent with the lower estimate on the
578 cessation of the lunar dynamo (e.g., Mighani et al. 2020). **The trends**
579 **outlined in Fig. 4 that arise from variations in k_c , [K], [S], and Q_c continue**
580 **under all other BMO boundary conditions.**

581
582 3.2.2. Influence of the Core's Heat Budget and Thermal Conductivity
583

584 The duration and intensity of the core dynamo are also sensitive to k_c ,
585 Q_c , and [K] (Figure 4). A potassium abundance of 50 ppm in the core
586 contributes thermal energy to the dynamo but suppresses growth of the inner
587 core, which can decrease the predicted intensity of the magnetic field
588 overall. Decreasing [K] has a minimal effect on the field intensity because
589 radiogenic heating is nearly equivalent to secular cooling in the dissipation
590 budget. In contrast, increasing the total heat flow to 1–2 GW increases the
591 duration and strength of the core-hosted dynamo, unless a low sulfur
592 abundance leads to rapid core solidification. Furthermore, the duration and
593 intensity of the field generally increases with decreasing thermal
594 conductivity values. We find that purely thermal convection typically occurs
595 before the onset of inner core crystallization if the thermal conductivity is
596 low (i.e., $10\text{--}30 \text{ W m}^{-1} \text{ K}^{-1}$ as in Fig. 3c). As thermal conductivity decreases,
597 the super-adiabatic heat flow increases, leading to a stronger, more long-
598 lived dynamo. Thermal convection-driven dynamos typically occur
599 simultaneously with BMO-hosted dynamos as the core is still hot and fully
600 molten. Compared to the abundance of sulfur in the bulk core, our simulations
601 reveal that small variations in parameters such as k_c , Q_c , and [K] play an

602 overall negligible role in the onset of a compositionally-driven dynamo,
603 whereas a thermal convection-driven dynamo is largely dictated by k_c .

604

605 3.2.3. Strength and Timing of the Core Dynamo

606

607 Depending on the BMO boundary condition, inner core crystallization can
608 produce fields ~ 0.7 – 2.3 Gyr in duration, with peak magnetic fields of 0.16,
609 0.45, 0.77, and 4 μT , for the ML, CIA, BF, and MAC scaling laws respectively
610 (Table 2). **A general issue arises in the case of the CIA, ML, and BF scalings**
611 **laws in which the strengths are not sufficiently strong enough to reproduce**
612 **the first period of decline to ~ 4 – 7 μT by 3.19 Ga (e.g., Strauss et al. 2021)**
613 **or the second period of decline to $\sim 5 \pm 2$ μT by ~ 1 – 2 Ga (e.g., Tikoo et al.**
614 **2017, Mighani et al. 2020). However, intensities ranging from ~ 1.7 – 4 μT can**
615 **be achieved under all BMO boundary conditions if the MAC scaling law is**
616 **assumed. In particular, an intensity of 4 μT is achieved if the BMO boundary**
617 **condition contains a lower fraction of radioactive material concentrated in**
618 **the BMO (i.e., V19K50p36). However, the magnetic field peaks to ~ 4 μT at ~ 2**
619 **Gyr after accretion, which is ~ 0.7 Gyr later than what is predicted from**
620 **paleomagnetic analyses (Strauss et al. 2021).**

621 Surface magnetic fields are weaker if they are driven by thermal
622 convection rather than by inner core crystallization. The peak surface
623 magnetic field driven by thermal convection in the nominal core model is
624 0.003 μT for the MAC scaling law, with **null fields predicted by all other**
625 **scaling laws (Table 2) since the total dissipation is subcritical (i.e., Φ_{CMB}**
626 **< 0 W). For all BMO boundary conditions, thermal convection in the core is**
627 **initiated ~ 3.7 Gyr ago (albeit briefly in some models; e.g., Fig. 3a).**
628 **Furthermore, depending on the BMO boundary condition, thermal convection can**
629 **persist intermittently for up to ~ 1.7 Gyr, resulting in an overlap with the**
630 **BMO-hosted field (e.g., Fig. 3c). **Thermal convection produces intensities****
631 **that are consistent with previous modeled estimates of the core (e.g.,**
632 **Laneuville et al. 2014, Evans et al. 2018, Scheinberg et al. 2015), but**
633 **inconsistent with paleomagnetic analyses constraining the initial and final**
634 **decline of the lunar dynamo (e.g., Tikoo et al. 2017, Mighani et al. 2020,**
635 **Strauss et al. 2021). Furthermore, these results are consistent with a low-**
636 **intensity epoch that persisted from ~ 1.9 – 0.8 Ga (e.g., Mighani et al. 2020,**
637 **Tikoo et al. 2017, Tikoo et al. 2014, Strauss et al. 2021).**

638 An uneven heat flow across the CMB may make the magnetic field
639 intermittent because dynamos can be sensitive to slight variations in heat

640 flow (Scheinberg et al. 2015). As an artifact of our modeling approach, early
641 magnetic fields produced via thermal convection are discontinuous due to
642 fluctuations in the Q_{CMB} from mantle dynamics. In some cases, thermal
643 convection generates fields that are predicted to drop to zero multiple times
644 before rising again from inner core crystallization. The duration of these
645 gaps in the magnetic field are much longer than the magnetic diffusion time
646 (Appendix C). Using the nominal models but with core conductivity lowered to
647 $k_c = 30 \text{ W m}^{-1} \text{ K}^{-1}$ as an example case (i.e., Fig 3c), gaps in thermal convection
648 on average last ~ 140 Myr, whereas the magnetic diffusion time is only a few
649 hundred years. Alternatively, dynamos induced by thermal convection can
650 transition directly into those induced by inner core crystallization,
651 compounding the resultant fields.

652

653 3.3. Monitoring the Sulfur Content of the Outer Core

654

655 **Our models assume that the lunar core always contains sub-eutectic**
656 **amounts of sulfur. We verified that this assumption is consistent with our**
657 **results, which track the sulfur content of the outer core over time (e.g.,**
658 **Figure 2c). For example, the eutectic is reached at sulfur abundances of ~ 24**
659 **wt.% at 5 GPa (e.g., Buono & Walker 2011, Breuer et al. 2015). In our models,**
660 **sulfur is less concentrated in the outer core unless the inner core is very**
661 **large. The inner core only grows so large in models where the bulk sulfur**
662 **content is low, which enables solidification at higher temperatures. Sulfur**
663 **reaches higher concentrations in the outer core in models that start with**
664 **lower amounts of sulfur in the bulk core. We found that the outer core stays**
665 **on the sulfur-poor side of the eutectic in all our models with bulk sulfur**
666 **contents of $> 5\text{--}7.5$ wt.%. The outer core can reach super-eutectic sulfur**
667 **contents if the bulk sulfur content is lower, but only for some BMO boundary**
668 **conditions and combinations of other parameters (e.g., low radiogenic heating**
669 **and relatively rapid cooling of the core). However, these conditions are only**
670 **reached in recent times, when we predict that the dynamo has already died.**
671 **Overall, our models capture the mode of core crystallization that probably**
672 **prevailed for most of lunar history. Section 4.1 below discusses some**
673 **complexities that future studies could include.**

674

675

676 3.4. Local Rossby Number

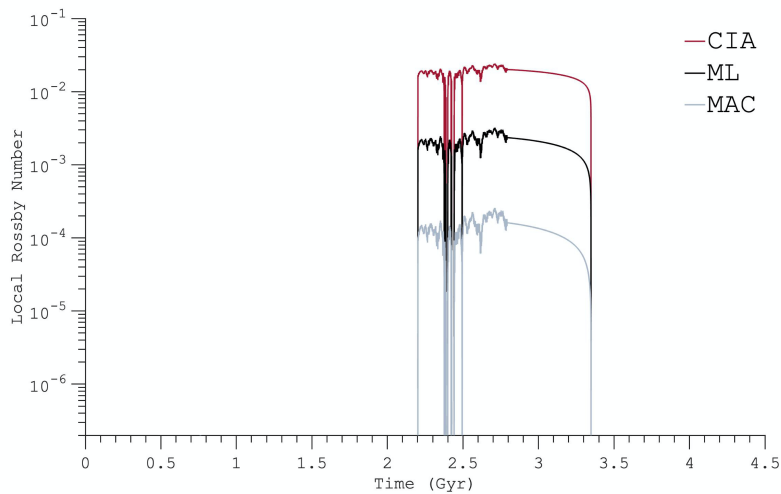
677

678

In order to make initial predictions for the magnetic field morphologies in our models, we estimate the local Rossby number as a proxy for whether the core dynamos would be dipole-dominated or multipolar, as for

679 example has been done previously for Ganymede’s dynamo (Rückriemen et al.
 680 2015). The CIA scaling law predicts higher values of the local Rossby number
 681 ($Ro_l \sim 10^{-2}$) relative to the ML ($Ro_l \sim 10^{-3}$) and MAC ($Ro_l \sim 10^{-4}$) scaling laws
 682 since inertia plays a larger role in the force balance (Christensen & Aubert
 683 2006). However, for the nominal core model, all scaling laws predict that the
 684 local Rossby number is below the threshold value of ~ 0.1 throughout the
 685 lifetime of the core dynamo, suggesting a prevailing dipole-dominated
 686 magnetic field (Table 2 and Figure 5).

687



697 Figure 5: Predictions of the local Rossby number for the nominal core model
 698 estimated from CIA, ML, and MAC scaling laws.

699
 700
 701

4. DISCUSSION

702 In this study, we demonstrated that a BMO dynamo naturally dovetails
 703 with a core dynamo. **Our models, in combination with the BMO models in**
 704 **Scheinberg et al. (2018), can reproduce the timing of the lunar magnetic**
 705 **field** and the surface field strength reduction over time. Future studies
 706 should explore at least four important issues.

707

4.1. Other Modes of Crystallization in the Core

708

709
 710 Future studies could model more complex modes of crystallization in the
 711 lunar core. To recap, we made two relevant assumptions. First, we assumed
 712 that the core always contains sub-eutectic amounts of sulfur, which most of
 713 our models indeed predict (section 3.3). Second, we assumed that the core
 714 solidifies from the center outwards. We set the liquidus temperature to

715 increase faster than the adiabatic temperature with pressure (e.g., with
716 gradients of 30 K/GPa versus ~23–25 K/GPa, respectively).

717 Future studies could relax these two assumptions, which would produce
718 more complicated behavior in models (e.g., Hauck et al. 2006). First, FeS
719 rather than Fe could crystallize from the outer core as it cooled if the
720 sulfur content were super-eutectic. Being sulfur-rich compared to the
721 residual liquid, solid FeS would float to the top of the liquid rather than
722 sink to form an inner core like solid Fe. Second, solidification could occur
723 at the top or middle of the outer core, rather than at its bottom. For
724 example, **“iron snow” could occur in metallic cores if the liquidus crosses**
725 **the adiabat above the base of the outer core. This process could help drive a**
726 **dynamo as the solidified iron sinks and remelts in the warmer fluid below,**
727 **leading to compositional convection (e.g., Williams 2009, Breuer et al.**
728 **2015).** Whether the Moon’s core entered an FeS crystallization or Fe snow
729 regime at any time remains an ongoing question.

730 Scientists might make more realistic models of the thermal evolution of
731 sulfur-rich cores if they include these processes. Such models require
732 detailed phase diagrams for the Fe-FeS system. The neglect of Fe snow and FeS
733 crystallization in our models does not change our takeaway message, however,
734 that the presence of a basal magma ocean overlying the core may influence the
735 timing and intensity of the core dynamo. Our models may interface with
736 future, more detailed descriptions of Fe snow and FeS in the core.

737

738 4.2. Morphology of the Lunar Dynamo

739

740 The geometry and paleo-orientation of the Moon’s magnetic field remains
741 largely uncertain. Estimates of paleoinclinations from five Apollo samples
742 suggest the existence of a dipolar field and a paleopole located at ~75°N
743 between 3.8 and 3.3 billion years ago (e.g., Cournède et al. 2012). These
744 findings are possibly best explained with a paleofield geometry close to the
745 present-day rotation axis of the Moon. Assumptions of the paleopole were made
746 based on the location of Apollo samples: samples collected from the northern
747 hemisphere were given a positive declination while samples collected from the
748 southern hemisphere were given a negative declination. However, the sign of
749 the inclination remains largely unknown and more data is required to confirm
750 interpretations made from lunar samples. Studies of Apollo 17 mare basalts
751 estimated an inclination of ~34° based on the layering of its parent boulder
752 (Nichols et al. 2021). This inclination is consistent with, but does not
753 require, a dipole in the center of the Moon aligned along its rotation axis.

793 dynamo region may effectively be the top of the BMO, rather than the top of
794 the core, even if the magnetic Reynolds number of the BMO is subcritical for
795 dynamo action.

796 Second, fluid flows within the BMO may also modulate the core field
797 itself (e.g., Gómez-Pérez et al. 2010). Conversely, if the BMO fluid is
798 stably-stratified, its presence may still filter out small-scale components
799 of the core field that rapidly vary via the magnetic skin effect (e.g.,
800 Christensen 2006). Third, the BMO may have resulted in larger magnetic
801 coupling between the core-mantle in the past, relevant to studies of the
802 Moon's rotational dynamics over time (e.g., Dumberry & Wieczorek 2016).
803 Further work, such as numerical dynamo modeling, is needed to better
804 understand the full degree of coupling between the BMO and core of the Moon.

805

806

4.4. Thermal Stratification in the Core

807 **The effects of thermal stratification in the lunar core are not**
808 **considered in this study. The inclusion of thermal stratification can have**
809 **several effects on the heat flux at the CMB. Studies of Mercury's core (e.g.,**
810 **Knibbe and Westrenen 2018, Knibbe and van Hoolst 2021) found that thermal**
811 **stratification can lead to an increased inner core size, higher temperatures,**
812 **and a larger heat flux at the CMB, which together results in an early start to**
813 **the magnetic field. Subsequent heat released upon core solidification would**
814 **enable slow core growth and an active magnetic field until present day.**
815 **Future work could apply these models of Mercury to the Moon.**

816

5. CONCLUSIONS

817

818 Our model for the coupled evolution of a basal magma ocean and the core
819 places estimates on the abundance of sulfur in the core (**i.e., 6.5–8.5 wt%**
820 **for the nominal core models**) and can explain the timing and relative
821 intensity of the lunar magnetic field consistent with other models of the
822 lunar core (e.g., Laneuville et al. 2014, Evans et al. 2018, Scheinberg et
823 al. 2015). The predicted timing of the lunar dynamo in our models is most
824 consistent with observational constraints when moderate abundances of sulfur
825 and potassium are assumed in the core, the core's thermal conductivity is
826 high, and if the present-day CMB heat flow is assumed to be low (or even
827 zero). Excessively high values of Q_{CMB} at present day (i.e., 1–2 GW) tends to
828 increase the duration of the magnetic fields longer than is consistent with
829 timing constraints on the end of the lunar dynamo (e.g., Mighani et al.

830 2020). Modeled intensities are most consistent with paleomagnetic analyses
831 constraining the initial and final decline of the lunar dynamo (e.g., Tikoo
832 et al. 2017, Mighani et al. 2020, Strauss et al. 2021) when the BMO boundary
833 condition is assumed to have less radiogenic heating concentrated in the BMO
834 or when the MAC scaling is assumed. Other scaling laws (i.e., CIA, ML, and
835 BF) predict that magnetic field intensities would be ~1–2 orders of magnitude
836 weaker at the surface than inferred from paleomagnetic data (although recall
837 that our intensities may be higher if electrical conductivity of the BMO is
838 taken into account).

839 Thermal convection can briefly exist with the BMO, but is generally
840 short-lived (Fig 3a) or intermittent (Fig 3c), generating magnetic field
841 intensities of up to ~0.3 μT that persist for $\lesssim 1.7$ Gyr. Near cessation of the
842 lunar BMO dynamo, heat flows are too low for purely thermal convection and
843 later dynamo action requires inner core crystallization. Magnetic fields
844 generated from the onset of inner core crystallization can reach intensities
845 of up to ~4 μT and can persist for $\lesssim 2.3$ Gyr. Temporal gaps may arise between
846 dynamos powered by different types of energy in the core (i.e., thermal vs.
847 compositional), which are neither confirmed nor excluded by extant data.
848 Temporal gaps in the magnetic field can lead to complications in
849 interpretations of the paleomagnetic record and may indicate that a portion
850 of Apollo samples with null paleointensities (e.g., Tarduno et al. 2021) may
851 not result from poor magnetic recording properties.

852 Estimates of the core sulfur abundance from our model can further
853 translate into predictions of the radius of the inner core. These predictions
854 can be verified with future missions, such as the Farside Seismic Suite
855 (e.g., Panning et al. 2021), which will provide new constraints on the
856 internal structure of the Moon, and the Lunar Geophysical Network (e.g.,
857 Weber et al. 2021), which aims to understand the size, state, and composition
858 of the lunar core and the chemical and physical stratification of the mantle.
859 Together, these findings will help discriminate between hypotheses that seek
860 to explain the high–low intensity epoch. Research on the Moon’s magnetic
861 history should remain fruitful for decades.

862

863

6. ACKNOWLEDGMENTS

864 This material is based upon work supported by the National Science Foundation
865 Graduate Research Fellowship under Grant No. 026257-001. We thank Aaron
866 Scheinberg for providing the complete outputs of published simulations.

867

868

- 870 Berrada, M., Secco, R. A., Yong, W., & Littleton, J. A. H. (2020). Electrical
871 Resistivity Measurements of Fe-Si With Implications for the Early Lunar
872 Dynamo. *Journal of Geophysical Research: Planets*, 125(7), 1–15.
873 <https://doi.org/10.1029/2020JE006380>
- 874 Bland, M. T., Showman, A. P., & Tobie, G. (2008). The production of
875 Ganymede's magnetic field. *Icarus*, 198(2), 384–399.
876 <https://doi.org/10.1016/j.icarus.2008.07.011>
- 877 Blaske, C. H., & O'Rourke, J. G. (2021). Energetic Requirements for Dynamos
878 in the Metallic Cores of Super-Earth and Super-Venus Exoplanets. *Journal of*
879 *Geophysical Research: Planets*, 126(7), 1–19.
880 <https://doi.org/10.1029/2020JE006739>
- 881 Breuer, D., Rueckriemen, T., & Spohn, T. (2015). Iron snow, crystal floats,
882 and inner-core growth: modes of core solidification and implications for
883 dynamos in terrestrial planets and moons. *Progress in Earth and Planetary*
884 *Science*, 2(1). <https://doi.org/10.1186/s40645-015-0069-y>
- 885 Bullard, E. C. (1949). The magnetic field within the earth. *Proceedings of*
886 *the Royal Society of London. Series A. Mathematical and Physical Sciences*,
887 197(1051), 433–453. <https://doi.org/10.1098/rspa.1949.0074>
- 888 Bullen, K. E. (1954). On the Homogeneity, or Otherwise, of the Earth's Upper
889 Mantle. *American Geophysical Union*, 33(5).
890 <https://doi.org/10.1029/TR035i005p00838>.
- 891 Buono, A. S., & Walker, D. (2011). The Fe-rich liquidus in the Fe-FeS system
892 from 1bar to 10GPa. *Geochimica et Cosmochimica Acta*, 75(8), 2072–2087.
893 <https://doi.org/10.1016/j.gca.2011.01.030>
- 894 Cameron, A. G. W. (1973). Abundances of the Elements in the Solar System.
895 *Space Science Reviews*, 15, 121–146.
- 896 Canup, R. M. (2012). Forming a Moon with an Earth-like Composition via a
897 Giant Impact. *Science*, 338(6110), 1052–1055.
898 <https://doi.org/10.1126/science.1226073>.
- 899 Chen, B., Li, J., & Hauck, S. A. (2008). Non-ideal liquidus curve in the Fe-S
900 system and Mercury's snowing core. *Geophysical Research Letters*, 35(7), 10–
901 14. <https://doi.org/10.1029/2008GL033311>
- 902 Christensen, U. R. (2006). A deep dynamo generating Mercury's magnetic field.
903 *Nature*, 444(7122), 1056–1058.
904
- 905 Christensen, U. R., & Aubert, J. (2006). Scaling properties of convection-
906 driven dynamos in rotating spherical shells and application to planetary
907 magnetic fields. *Geophysical Journal International*, 166(1), 97–114.
908 <https://doi.org/10.1111/j.1365-246X.2006.03009.x>
909
- 910 Christensen, U. R., Holzwarth, V., & Reiners, A. (2009). Energy flux
911 determines magnetic field strength of planets and stars. *Nature*, 457(7226),
912 167–169. <https://doi.org/10.1038/nature07626>

913
914 Christensen, U. r. (2010). Dynamo scaling laws and applications to the
915 planets. *Space science reviews*, 152(1), 565-590.
916 <https://doi.org/10.1007/s11214-009-9553-2>

917 Chudinovskikh, L., & Boehler, R. (2007). Eutectic melting in the system Fe-S
918 to 44 GPa. *Earth and Planetary Science Letters*, 257(1-2), 97-103.
919 <https://doi.org/10.1016/j.epsl.2007.02.024>

920 Cournède, C., Gattacceca, J., & Rochette, P. (2012). Magnetic study of large
921 Apollo samples: Possible evidence for an ancient centered dipolar field on
922 the Moon. *Earth and Planetary Science Letters*, 331-332, 31-42.
923 <https://doi.org/10.1016/j.epsl.2012.03.004>

924 Ćuk, M., Hamilton, D. P., & Stewart, S. T. (2019). Early dynamics of the
925 lunar core. *Journal of Geophysical Research: Planets*, 124(11), 2917-2928.
926

927 Ćuk, M. & Stewart, S. T. (2012). Making the Moon from a Fast-Spinning Earth:
928 A Giant Impact Followed by Resonant Despinning. *Science*, 338(6110), 1047-
929 1052. <https://doi.org/10.1126/science.1225542>

930 Dasgupta, R., Buono, A., Whelan, G., & Walker, D. (2009). High-pressure
931 melting relations in Fe-C-S systems: Implications for formation, evolution,
932 and structure of metallic cores in planetary bodies. *Geochimica et*
933 *Cosmochimica Acta*, 73(21), 6678-6691.
934 <https://doi.org/10.1016/j.gca.2009.08.001>

935 Davies, C. J., & Pommier, A. (2018). Iron snow in the Martian core?. *Earth*
936 *and Planetary Science Letters*, 481, 189-200.
937 <https://doi.org/10.1016/j.epsl.2017.10.026>

938

939 Dumberry, M., & Wieczorek, M. A. (2016). The forced precession of the Moon's
940 inner core. *Journal of Geophysical Research: Planets*, 121(7), 1264-1292.

941 Dwyer, C. A., Stevenson, D. J., & Nimmo, F. (2011). A long-lived lunar dynamo
942 driven by continuous mechanical stirring. *Nature*, 479(7372), 212-214.
943 <https://doi.org/10.1038/nature10564>

944 Dygert, N., Lin, J. F., Marshall, E. W., Kono, Y., & Gardner, J. E. (2017). A
945 Low Viscosity Lunar Magma Ocean Forms a Stratified Anorthitic Flotation Crust
946 With Mafic Poor and Rich Units. *Geophysical Research Letters*, 44(22), 11,282-
947 11,291. <https://doi.org/10.1002/2017GL075703>

948 Elardo, S. M., Draper, D. S., & Shearer, C. K. (2011). Lunar Magma Ocean
949 crystallization revisited: Bulk composition, early cumulate mineralogy, and
950 the source regions of the highlands Mg-suite. *Geochimica et Cosmochimica*
951 *Acta*, 75(11), 3024-3045. <https://doi.org/10.1016/j.gca.2011.02.033>

952 Elsasser, W. M. (1950). The Earth's Interior and Geomagnetism. *Reviews of*
953 *Modern Physics*, 22(1). <https://doi.org/10.1103/RevModPhys.22.1>.

954 Elkins-Tanton, L. T., & Grove, T. L. (2011). Water (hydrogen) in the lunar
955 mantle: Results from petrology and magma ocean modeling. *Earth and Planetary*
956 *Science Letters*, 307(1-2), 173-179.
957 <https://doi.org/10.1016/j.epsl.2011.04.027>

- 958 Elkins-Tanton, L. T., Burgess, S., & Yin, Q. Z. (2011). The lunar magma
959 ocean: Reconciling the solidification process with lunar petrology and
960 geochronology. *Earth and Planetary Science Letters*, 304(3–4), 326–336.
961 <https://doi.org/10.1016/j.epsl.2011.02.004>
- 962 Evans, A. J., Zuber, M. T., Weiss, B. P., & Tikoo, S. M. (2014). A wet,
963 heterogeneous lunar interior: Lower mantle and core dynamo evolution. *Journal*
964 *of Geophysical Research E: Planets*, 119(5), 1061–1077.
965 <https://doi.org/10.1002/2013JE004494>
- 966 Evans, A. J., & Tikoo, S. M. (2022). An episodic high-intensity lunar core
967 dynamo. *Nature Astronomy*. <https://doi.org/10.1038/s41550-021-01574-y>
- 968 Evans, A. J., Tikoo, S. M., & Andrews-Hanna, J. C. (2018). The Case Against
969 an Early Lunar Dynamo Powered by Core Convection. *Geophysical Research*
970 *Letters*, 45(1), 98–107. <https://doi.org/10.1002/2017GL075441>
- 971 Fei, Y., Bertka, C. M., & Finger, L. W. (1997). High-pressure iron-sulfur
972 compound, Fe₃S₂, and melting relations in the Fe-FeS system. *Science*,
973 275(5306), 1621–1623. <https://doi.org/10.1126/science.275.5306.1621>
- 974 Fei, Y., Li, J., Bertka, C. M., & Prewitt, C. T. (2000). Structure type and
975 bulk modulus of Fe₃S, a new iron-sulfur compound. *American Mineralogist*,
976 85(11–12), 1830–1833. <https://doi.org/10.2138/am-2000-11-1229>
- 977 Garcia, R. F., Gagnepain-Beyneix, J., Chevrot, S., & Lognonné, P. (2011).
978 Very preliminary reference Moon model. *Physics of the Earth and Planetary*
979 *Interiors*, 188(1–2), 96–113. <https://doi.org/10.1016/j.pepi.2011.06.015>
- 980 Glatzmaier, G. A., & Roberts, P. H. (1995). A three-dimensional convective
981 dynamo solution with rotating and finitely conducting inner core and mantle.
982 *Physics of the Earth and Planetary Interiors*, 91(1–3), 63–75.
983 [https://doi.org/10.1016/0031-9201\(95\)03049-3](https://doi.org/10.1016/0031-9201(95)03049-3)
- 984
985 Gómez-Pérez, N., Heimpel, M., & Wicht, J. (2010). Effects of a radially
986 varying electrical conductivity on 3D numerical dynamos. *Physics of the Earth*
987 *and Planetary Interiors*, 181(1–2), 42–53.
- 988 Hamid, S. H., & O'Rourke, J. G. (2022). Modeling of the Lunar Magma Ocean.
989 In: Cudnik B. (eds) *Encyclopedia of Lunar Science*. Springer, Cham.
- 990 Hartmann, William, K., & Davis, D. R. (1975). Satellite-Sized Planetesimals
991 and Lunar Origin. *Icarus*, 24, 504–515.
- 992 Hauck, S. A., Aurnou, J. M., & Dombard, A. J. (2006). Sulfur's impact on core
993 evolution and magnetic field generation on Ganymede. *Journal of Geophysical*
994 *Research E: Planets*, 111(9), 1–14. <https://doi.org/10.1029/2005JE002557>
- 995 Hess, P. C., & Parmentier, E. M. (1995). A model for the thermal and chemical
996 evolution of the Moon's interior: implications for the onset of mare
997 volcanism. *Earth and Planetary Science Letters*, 134(3–4), 501–514.
998 [https://doi.org/10.1016/0012-821X\(95\)00138-3](https://doi.org/10.1016/0012-821X(95)00138-3)

- 999 Hirose, K., Labrosse, S., Herlund, J. (2013). Composition and State of the
1000 Core. *Annual Review of Earth and Planetary Sciences*, 41(1), 657–691.
1001 <https://doi.org/10.1146/annurev-earth-050212-124007>.
- 1002 Hood, L. L., Mitchell, D. L., Lin, R. P., Acuna, M. H., & Binder, A. B.
1003 (1999). Initial measurements of the lunar induced magnetic dipole moment
1004 using lunar prospector magnetometer data. *Geophysical Research Letters*,
1005 26(15), 2327–2330. <https://doi.org/10.1029/1999GL900487>
- 1006 Kageyama, A., Sato, T., Watanabe, K., Horiuchi, R., Hayashi, T., Todo, Y.,
1007 Watanabe, T. H., & Takamaru, H. (1995). Computer simulation of a
1008 magnetohydrodynamic dynamo. II. *Physics of Plasmas*, 2(5), 1421–1431.
1009 <https://doi.org/10.1063/1.871485>
- 1010 Khan, A., Connolly, J. A. D., Pommier, A., & Noir, J. (2014). Geophysical
1011 evidence formelt in the deep lunar interior and implications for lunar
1012 evolution. *Journal of Geophysical Research E: Planets*, 119(10), 2197–2221.
1013 <https://doi.org/10.1002/2014JE004661>
- 1014 Khan, A., Liebske, C., Rozel, A., Rivoldini, A., Nimmo, F., Connolly, J. A.
1015 D., Plesa, A. C., & Giardini, D. (2018). A Geophysical Perspective on the
1016 Bulk Composition of Mars. *Journal of Geophysical Research: Planets*, 123(2),
1017 575–611. <https://doi.org/10.1002/2017JE005371>
- 1018 Labrosse, S. (2014). Thermal evolution of the core with a high thermal
1019 conductivity. *Physics of the Earth and Planetary Interiors*, 247, 36–55.
1020 <https://doi.org/10.1016/j.pepi.2015.02.002>
- 1021 Laneuville, M., Wieczorek, M. A., Breuer, D., Aubert, J., Morard, G., &
1022 Rückriemen, T. (2014). A long-lived lunar dynamo powered by core
1023 crystallization. *Earth and Planetary Science Letters*, 401, 251–260.
1024 <https://doi.org/10.1016/j.epsl.2014.05.057>
- 1025 Le Bars, M., Wieczorek, M. A., Karatekin, A., Cébron, D., & Laneuville, M.
1026 (2011). An impact-driven dynamo for the early Moon. *Nature*, 479(7372), 215–
1027 218. <https://doi.org/10.1038/nature10565>
- 1028 Lee, K. K. M., Steinle-Neumann, G., & Jeanloz, R. (2004). Ab-initio high-
1029 pressure alloying of iron and potassium: Implications for the Earth's core.
1030 *Geophysical Research Letters*, 31(11), 1–4.
1031 <https://doi.org/10.1029/2004GL019839>
- 1032 Meyer, J., & Wisdom, J. (2011). Precession of the lunar core. *Icarus*, 211(1),
1033 921–924. <https://doi.org/10.1016/j.icarus.2010.09.016>
- 1034 Mighani, S., wang, H., Shuster, D. L., Cauê, S. B., Nichols, C. I. O., &
1035 Weiss, B. P. (2020). The end of the lunar dynamo. *Science Advances*, 6, 1–8.
- 1036 Morard, G., Sanloup, C., Fiquet, G., Mezouar, M., Rey, N., Poloni, R., &
1037 Beck, P. (2007). Structure of eutectic Fe-FeS melts to pressures up to 17
1038 GPa: Implications for planetary cores. *Earth and Planetary Science Letters*,
1039 263(1–2), 128–139. <https://doi.org/10.1016/j.epsl.2007.09.009>
- 1040 Morard, G., Andrault, D., Guignot, N., Sanloup, C., Mezouar, M., Petitgirard,
1041 S., & Fiquet, G. (2008). In situ determination of Fe-Fe₃S phase diagram and

- 1042 liquid structural properties up to 65 GPa. *Earth and Planetary Science*
1043 *Letters*, 272(3–4), 620–626. <https://doi.org/10.1016/j.epsl.2008.05.028>
- 1044 Murthy, V. R., Van Westrenen, W., & Fei, Y. (2003). Experimental evidence
1045 that potassium is a substantial radioactive heat source in planetary cores.
1046 *Nature*, 423(6936), 163–165. <https://doi.org/10.1038/nature01560>
- 1047 Nakajima, M., & Stevenson, D. J. (2014). Investigation of the dynamol state
1048 of the Moon-forming disk: Bridging SPH simulations and hydrostatic models.
1049 *Icarus*, 233, 259–267. <https://doi.org/10.1016/j.icarus.2014.01.008>
- 1050 Nayak, M., Hemingway, D., & Garrick-Bethell, I. (2017). Magnetization in the
1051 South Pole-Aitken basin: Implications for the lunar dynamo and true polar
1052 wander. *Icarus*, 286, 153–192. <https://doi.org/10.1016/j.icarus.2016.09.038>
- 1053 Nemchin, A., Timms, N., Pidgeon, R., Geisler, T., Reddy, S., & Meyer, C.
1054 (2009). Timing of crystallization of the lunar magma ocean constrained by the
1055 oldest zircon. *Nature Geoscience*, 2(2), 133–136.
1056 <https://doi.org/10.1038/ngeo417>.
- 1057 Nichols, C. I. O., Weiss, B. P., Getzin, B. L., Schmitt, H. H., Béguin, A.,
1058 Rae, A. S. P., & Shah, J. (2021). The palaeoinclination of the ancient lunar
1059 magnetic field from an Apollo 17 basalt. *Nature Astronomy*, 5(12), 1216–1223.
1060 <https://doi.org/10.1038/s41550-021-01469-y>
- 1061 Nimmo, F. (2015). Energetics of the core, *Treatise on Geophysics*, Vol. 8, pp.
1062 27–55.
- 1063 Olson, P., Christensen, & U. R. (2006). Dipole Moment Scaling for Convection-
1064 Driven Planetary Dynamos. *Earth and Planetary Science Letters*, 250(3–4), 561–
1065 571. <https://doi.org/10.1016/j.epsl.2006.08.008>.
- 1066 Oliveira, J. S., & Wieczorek, M. A. (2017). Testing the axial dipole
1067 hypothesis for the Moon by modeling the direction of crustal magnetization.
1068 *Journal of Geophysical Research: Planets*, 122(2), 383–399.
1069 <https://doi.org/10.1002/2016JE005199> Oliveira
- 1070 Panning, M. P., Kedar, S., Bowles, N., Calcutt, S., Cutler, J., Elliott, J.
1071 O., Garcia, R. F., Kawamura, T., Lognonné, P. H., Miller, E. A., Nunn, C.,
1072 Pike, W. T., Pont, G., De Raucourt, S., Standley, I. M., Walsh, W., Weber, R.
1073 C., & Yana, C. (2021) Farside Seismic Suite (FSS): First seismic data from
1074 the farside of the Moon delivered by a commercial lander. *American*
1075 *Geophysical Union Fall Meeting*, Abstract #839546.
- 1076 Pommier, A. (2018). Influence of sulfur on the electrical resistivity of a
1077 crystallizing core in small terrestrial bodies. *Earth and Planetary Science*
1078 *Letters*, 496, 37–46. <https://doi.org/10.1016/j.epsl.2018.05.032>
- 1079 Pommier, A., Davies, C. J., Zhang, R. (2020). A Joint Experimental-Modeling
1080 Investigation of the Effect of Light Elements on Dynamos in Small Planets and
1081 Moons. *Journal of Geophysical Research: Planets*, 125, e2020JE006492.
1082 <https://doi.org/10.1029/2020JE006492>

- 1083 Roberts, P.H., 2007. Theory of the geodynamo. In: Schubert, G. (Ed.),
1084 Treatise on Geophysics, vol. 8. Core Dynamics. Elsevier, Amsterdam, pp. 67–
1085 105. Ch. 3. <https://doi.org/10.1016/B978-044452748-6.00133-4>.
- 1086 Rückriemen, T., Breuer, D., & Spohn, T. (2015). The Fe snow regime in
1087 Ganymede's core: A deep-seated dynamo below a stable snow zone. *Journal of*
1088 *Geophysical Research E: Planets*, 120(6), 1095–1118.
1089 <https://doi.org/10.1002/2014JE004781>
- 1090 Rzehak, R. L., Sebastian, K., Liam, H., Florian, K., Peter, S., P, L. F., &
1091 C, F. R. O. (2022). Redox-dependent Ti stable isotope fractionation on the
1092 Moon: implications for current lunar magma ocean models. *Contributions to*
1093 *Mineralogy and Petrology*, 177(8), 1–20. <https://doi.org/10.1007/s00410-022-01947-0>
- 1095 Rzehak, L. J. A., Kommescher, S., Kurzweil, F., Sprung, P., Leitzke, F. P., &
1096 Fonseca, R. O. C. (2021). The redox dependence of titanium isotope
1097 fractionation in synthetic Ti-rich lunar melts. *Contributions to Mineralogy*
1098 *and Petrology*, 176(3), 1–16. <https://doi.org/10.1007/s00410-020-01769-y>
- 1099 Scheinberg, A., Soderlund, K. M., & Schubert, G. (2015). Magnetic field
1100 generation in the lunar core: The role of inner core growth. *Icarus*, 254, 62–
1101 71. <https://doi.org/10.1016/j.icarus.2015.03.013>
- 1102 Scheinberg, A. L., Soderlund, K. M., & Elkins-Tanton, L. T. (2018). A basal
1103 magma ocean dynamo to explain the early lunar magnetic field. *Earth and*
1104 *Planetary Science Letters*, 492, 144–151.
1105 <https://doi.org/10.1016/j.epsl.2018.04.015>
- 1106 Schubert, G. & Soderlund, K. M. (2011). Planetary magnetic fields:
1107 Observations and models. *Physics of the Earth and Planetary Interiors*, 187(3–
1108 4), 92–108. <https://doi.org/10.1016/j.pepi.2011.05.013>
- 1109 Shimizu, H., Matsushima, M., Takahashi, F., Shibuya, H., & Tsunakawa, H.
1110 (2013). Constraint on the lunar core size from electromagnetic sounding based
1111 on magnetic field observations by an orbiting satellite. *Icarus*, 222(1), 32–
1112 43. <https://doi.org/10.1016/j.icarus.2012.10.029>
- 1113 Soderlund, K. M., & Stanley, S. (2020). The underexplored frontier of ice
1114 giant dynamos. *Philosophical Transactions of the Royal Society A*, 378(2187),
1115 20190479. <https://doi.org/10.1098/rsta.2019.0479>
- 1116 Steenstra, E. S., Rai, N., Knibbe, J. S., Lin, Y. H., & van Westrenen, W.
1117 (2016). New geochemical models of core formation in the Moon from metal–
1118 silicate partitioning of 15 siderophile elements. *Earth and Planetary Science*
1119 *Letters*, 441, 1–9. <https://doi.org/10.1016/j.epsl.2016.02.028>
- 1120 Steenstra, E. S., Agmon, N., Berndt, J., Klemme, S., Matveev, S., & Van
1121 Westrenen, W. (2018). Depletion of potassium and sodium in mantles of Mars,
1122 Moon and Vesta by core formation. *Scientific Reports*, 8(1), 1–10.
1123 <https://doi.org/10.1038/s41598-018-25505-6>.
- 1124 Stegman, D. R., Jellinek, A. M., Zatman, S. A., Baumgardner, J. R., &
1125 Richards, M. A. (2003). An early lunar core dynamo driven by thermochemical

- 1126 mantle convection. *Nature*, 421(6919), 143–146.
1127 <https://doi.org/10.1038/nature01267>
- 1128 Stevenson, D. J. (2003). Planetary magnetic fields. *Earth and Planetary*
1129 *Science Letters*, 208(1–2), 1–11. [https://doi.org/10.1016/S0012-821X\(02\)01126-](https://doi.org/10.1016/S0012-821X(02)01126-3)
1130 3
- 1131 Stevenson, D. J. (1983). Planetary magnetic fields. *Reports on Progress in*
1132 *Physics*, 46(5), 555–620. <https://doi.org/10.1088/0034-4885/46/5/001>
- 1133 Stewart, A. J., Schmidt, M. W., Westrenen, W. Van, & Liebske, C. (2007).
1134 *Mars: A New Core-Crystallization Regime*. 316(June), 1323–1326.
- 1135 Stixrude, L., Scipioni, R., & Desjarlais, M. P. (2020). A silicate dynamo in
1136 the early Earth. *Nature Communications*, 11(1), 6–10.
1137 <https://doi.org/10.1038/s41467-020-14773-4>
- 1138 Strauss, B. E., Tikoo, S. M., Gross, J., Setera, J. B., & Turrin, B. (2021).
1139 Constraining the Decline of the Lunar Dynamo Field at ≈ 3.1 Ga Through
1140 Paleomagnetic Analyses of Apollo 12 Mare Basalts. *Journal of Geophysical*
1141 *Research: Planets*, 126(3), 1–21. <https://doi.org/10.1029/2020JE006715>
1142
- 1143 Stys, C., & Dumberry, M. (2020). A past lunar dynamo thermally driven by the
1144 precession of its inner core. *Journal of Geophysical Research:*
1145 *Planets*, 125(7), e2020JE006396.
- 1146 Tarduno, J. A., Cottrell, R. D., Lawrence, K., Bono, R. K., Huang, W.,
1147 Johnson, C. L., Blackman, E. G., Smirnov, A. V., Nakajima, M., Neal, C. R.,
1148 Zhou, T., Ibanez-Mejia, M., Oda, H., & Crummins, B. (2021). Absence of a
1149 long-lived lunar paleomagnetosphere. *Science Advances*, 7(32), 1–15.
1150 <https://doi.org/10.1126/sciadv.abi7647>
- 1151 Tikoo, S. M., Weiss, B. P., Shuster, D. L., Suavet, C., Wang, H., & Grove, T.
1152 L. (2017). A two-billion-year history for the lunar dynamo. *Science Advances*,
1153 3(8), 1–10. <https://doi.org/10.1126/sciadv.1700207>
- 1154 Warren, P. (1985). The Magma Ocean Concept and Lunar Evolution. *Annual Review*
1155 *of Earth and Planetary Sciences*, 13(1), 201–240.
1156 <https://doi.org/10.1146/annurev.ea.13.050185.001221>
- 1157 Weber, R. C., Lin, P. Y., Garnero, E. J., Williams, Q., & Lognonné, P.
1158 (2011). Seismic detection of the lunar core. *Science*, 331(6015), 309–312.
1159 <https://doi.org/10.1126/science.1199375>
- 1160 Weber, R., Neal, C. R., Grimm, R., Grott, M., Schmerr, N., Wieczorek, M., ...
1161 Zuber, M. (2021). The scientific rationale for deployment of a long-lived
1162 geophysical network on the Moon. *Bulletin of the AAS*, 53(4).
1163 <https://doi.org/10.3847/25c2cf.674dcfdf>
- 1164 Weiss, B. P., & Tikoo, S. M. (2014). The lunar dynamo. *Science*, 346(6214).
1165 <https://doi.org/10.1126/science.1246753>
- 1166 Wieczorek, M. A., Jolliff, B. L., Khan, A., Pritchard, M. E., Weiss, B. P.,
1167 Williams, J. G., Hood, L. L., Richter, K., Neal, C. R., Shearer, C. K.,
1168 McCallum, I. S., Tompkins, S., Hawke, B. R., Peterson, C., Gillis, J. J., &

- 1169 Bussey, B. (2006). The constitution and structure of the Lunar interior.
 1170 *Reviews in Mineralogy and Geochemistry*, 60(November), 221–364.
 1171 <https://doi.org/10.2138/rmg.2006.60.3>
- 1172 Wieczorek, M., Weiss, B., Breuer, D., Cébron, D., Fuller, M., Garrick-
 1173 bethell, I., Gattacceca, J., Halekas, J., Hemingway, D., Hood, L., Wieczorek,
 1174 M., Weiss, B., Breuer, D., Cébron, D., Fuller, M., Wieczorek, M. A., Weiss,
 1175 B. P., Breuer, D., Cébron, D., & Fuller, M. (2022). *Lunar magnetism To cite*
 1176 *this version* : HAL Id : hal-03524536.
- 1177 Williams, J. G., Boggs, D. H., Yoder, C. F., Ratcliff, J. T., and Dickey, J.
 1178 O. (2001), Lunar rotational dissipation in solid body and molten core, *J.*
 1179 *Geophys. Res.*, 106(E11), 27933– 27968, doi:10.1029/2000JE001396.
- 1180 Williams, Q. (2009). Bottom-up versus top-down solidification of the cores of
 1181 small solar system bodies: Constraints on paradoxical cores. *Earth and*
 1182 *Planetary Science Letters*, 284(3–4), 564–569.
 1183 <https://doi.org/10.1016/j.epsl.2009.05.019>
- 1184 Williams, J. G., Konopliv, A. S., Boggs, D. H., Park, R. S., Yuan, D. N.,
 1185 Lemoine, F. G., Goossens, S., Mazarico, E., Nimmo, F., Weber, R. C., Asmar,
 1186 S. W., Jay Melosh, H., Neumann, G. A., Phillips, R. J., Smith, D. E.,
 1187 Solomon, S. C., Watkins, M. M., Wieczorek, M. A., Andrews-Hanna, J. C., ...
 1188 Zuber, M. T. (2014). Lunar interior properties from the GRAIL mission.
 1189 *Journal of Geophysical Research: Planets*, 119(7), 1546–1578.
 1190 <https://doi.org/10.1002/2013JE004559>
- 1191 Yin, Y., Li, Z., & Zhai, S. (2019). The phase diagram of the Fe-P binary
 1192 system at 3 GPa and implications for phosphorus in the lunar core. *Geochimica*
 1193 *et Cosmochimica Acta*, 254, 54–66. <https://doi.org/10.1016/j.gca.2019.03.037>
- 1194 Zhan, X., & Schubert, G. (2012). Powering Ganymede’s dynamo. *Journal of*
 1195 *Geophysical Research E: Planets*, 117(8), 1–7.
 1196 <https://doi.org/10.1029/2012JE004052>
- 1197 Ziegler, L. B., & Stegman, D. R. (2013). Implications of a long-lived basal
 1198 magma ocean in generating Earth’s ancient magnetic field. *Geochemistry,*
 1199 *Geophysics, Geosystems*, 14(11), 4735–4742.
 1200 <https://doi.org/10.1002/2013GC005001>

1201

1202

APPENDIX A. RADIAL STRUCTURE OF THE LUNAR CORE

1203

1204

We approximated the lunar core as a mixture of liquid Fe and liquid Fe-10
 1205 wt% S to make structure models. We followed the procedure detailed in Khan et
 1206 al. (2017), especially in their Appendix A, to calculate radial profiles of
 1207 density, pressure, and temperature. We use the mass-weighted averages of the
 1208 depth-dependent values of the Grüneisen parameter and the coefficient of
 1209 thermal expansion. We then performed a least-squares fit to parameterize the
 1210 radial density using a fourth-degree polynomial:

1211
$$\rho(r) = \rho_0 \left[1 - \left(\frac{r}{L_\rho} \right)^2 - A_\rho \left(\frac{r}{L_\rho} \right)^4 \right], \quad (A1)$$

1212 where ρ_0 is density at the center of the core, L_ρ is a length scale, and A_ρ is
 1213 a constant. The effective bulk modulus is then $K_0 = 2\pi G(L_\rho \rho_0)^2/3$, where G is
 1214 the gravitational constant. The derivative of the effective bulk modulus is K_1
 1215 $= (10 A_\rho + 13)/5$. Finally, the adiabatic thermal gradient in the core is then
 1216 $T_a(r) = T(0)[\rho(r)/\rho_0]^\gamma$.

1217

1218 APPENDIX B. ENERGETICS OF A DYNAMO IN THE LUNAR CORE

1219

1220 Section 2.2 describes the heat budget of the lunar core. For completeness,
 1221 we list here the polynomial equations used to calculate the different terms.
 1222 Analogous equations that were developed to model Earth's core can be found in
 1223 Labrosse (2015), albeit with slightly different notation and additional
 1224 complexities added to the analytic formulation, and in the Supporting
 1225 Information for Blaske & O'Rourke (2021).

1226 In our models, the total heat flow across the core/mantle boundary can be
 1227 partitioned into four different terms, each of which is proportional to the
 1228 overall cooling rate of the core (dT_{CMB}/dt). First, we have the heat flow
 1229 associated with secular cooling of the fluid portion of the core. Before the
 1230 inner core nucleates, we have

1231
$$\bar{Q}_S = -\frac{4}{3}\pi\rho_0 C_C L_\rho^3 f_c \left(\frac{R_C}{L_\rho}, \gamma \right) \left[1 - \left(\frac{R_C}{L_\rho} \right)^2 - A_\rho \left(\frac{R_C}{L_\rho} \right)^4 \right]^{-\gamma}, \quad (B1)$$

1232 where

1233
$$f_c(x, \delta) = x^3 \left[1 - \frac{3}{5}(\delta + 1)x^2 - \frac{3}{14}(\delta + 1)(2A_\rho - \delta)x^4 \right]. \quad (B2)$$

1234 After the inner core nucleates,

1235
$$\bar{Q}_S = -\frac{4}{3}\pi\rho_0 C_C L_\rho^3 \left[1 - \left(\frac{R_I}{L_\rho} \right)^2 - A_\rho \left(\frac{R_I}{L_\rho} \right)^4 \right]^{-\gamma} \left[\frac{dT_L}{dR_I} + \frac{2\gamma T_L(R_I) \left(\frac{R_I}{L_\rho} \right) \left(1 + 2A_\rho \left(\frac{R_I}{L_\rho} \right)^2 \right)}{1 - \left(\frac{R_I}{L_\rho} \right)^2 - A_\rho \left(\frac{R_I}{L_\rho} \right)^4} \right] \left[f_c \left(\frac{R_C}{L_\rho}, \gamma \right) \right. \\ \left. - f_c \left(\frac{R_I}{L_\rho}, \gamma \right) \right] \left(\frac{dR_I}{dT_C} \right), \quad (B3)$$

1237 where $T_L(R_I)$ is the liquidus temperature evaluated at the inner core boundary
 1238 given by

1239
$$T_L(R_I) = T_L(0) - K_0 \left(\frac{dT_L}{dP} \right) \left(\frac{R_I}{L_\rho} \right)^2 + \frac{c_0}{f_c \left(\frac{R_C}{L_\rho}, 0 \right)} \left(\frac{dT_L}{dc} \right) \left(\frac{R_I}{L_\rho} \right)^3. \quad (B4)$$

1240 Here c_o is the mass fraction of sulfur in the outer core, which increases as
 1241 the inner core grows. Differentiating this equation yields the slope of the
 1242 liquidus at the inner core boundary:

$$1243 \quad \frac{dT_L}{dR_I} = -2K_0 \left(\frac{dT_L}{dP} \right) \left(\frac{R_I}{L_\rho^2} \right) + \frac{3c_o}{f_c \left(\frac{R_C}{L_\rho}, 0 \right)} \left(\frac{dT_L}{dc} \right) \left(\frac{R_I^2}{L_\rho^3} \right). \quad (B5)$$

1244 Following Nimmo (2015), we use this slope and the adiabatic thermal gradient
 1245 to calculate the growth rate of the inner core

$$1246 \quad \frac{dR_I}{dT_C} = - \frac{1}{\left(\frac{dT_L}{dP} - \frac{dT_a}{dP} \right)_{R_I}} \left(\frac{T_L(R_I)}{T_{CMB} \rho(R_I) g(R_I)} \right). \quad (B6)$$

1247 The growth of the inner core also releases latent heat

$$1248 \quad \tilde{Q}_L = 4\pi R_I^2 \rho(R_I) T_L(R_I) \Delta S_C \left(\frac{dR_I}{dT_C} \right), \quad (B7)$$

1249 where $\Delta S_C = 200$ J/K/kg is the entropy of melting for the inner core (Nimmo
 1250 2015). Next, we compute the gravitational energy related to the exclusion of
 1251 sulfur from the inner core as it freezes:

$$1252 \quad \tilde{Q}_G = \frac{8\pi^2 G \rho_o c_o \alpha_I R_I^2 L_p^2}{f_c \left(\frac{R_C}{L_\rho}, 0 \right)} \left[f_\chi \left(\frac{R_C}{L_\rho} \right) - f_\chi \left(\frac{R_I}{L_\rho} \right) \right] \left(\frac{dR_I}{dT_C} \right), \quad (B8)$$

1253 where $\alpha_I = 2.3$ is the coefficient of compositional expansion for enriching the
 1254 outer core in sulfur (Nimmo 2015). Here we leverage another useful function:

$$1255 \quad f_\chi(x) = x^3 \left\{ -\frac{1}{3} \left(\frac{R_I}{L_\rho} \right)^2 + \frac{1}{2} \left[1 + \left(\frac{R_I}{L_\rho} \right)^2 \right] x^2 - \frac{13}{70} x^4 \right\}. \quad (B9)$$

1256 Last and easiest, the radiogenic heat in the core is

$$1257 \quad Q_R = M_C H_K [K] \exp(-\lambda_K t), \quad (B10)$$

1258 where $\lambda_K = 1.76 \times 10^{-17}$ s⁻¹ and $H_K = 4.2 \times 10^{-14}$ W/kg/ppm are the decay constant
 1259 and the heat production rate at $t = 0$ for potassium-40, respectively.

1260 The energy budget by itself does not reveal whether a dynamo may exist in
 1261 the lunar core. We must compute the dissipation budgets, again following
 1262 Labrosse (2015) and studies such as Blaske & O'Rourke (2021). First, we
 1263 expand equation 3 in the main text as

$$1264 \quad \Phi_{CMB} = \left(\frac{T_D [T_L(R_I) - T_{CMB}]}{T_L(R_I) T_{CMB}} \right) Q_L + \left(\frac{T_D}{T_{CMB}} \right) Q_G + \left(\frac{T_D - T_{CMB}}{T_{CMB}} \right) Q_R + \left(\frac{T_D (T_S - T_{CMB})}{T_S T_{CMB}} \right) Q_S - \Phi_K. \quad (B11)$$

1265 Here we use the average temperature in the outer core:

$$1266 \quad T_D = \frac{T(R_I)}{\left[1 - \left(\frac{R_I}{L_\rho} \right)^2 - A_\rho \left(\frac{R_I}{L_\rho} \right)^4 \right]^\gamma} \left[\frac{f_c \left(\frac{R_C}{L_\rho}, 0 \right) - f_c \left(\frac{R_I}{L_\rho}, 0 \right)}{f_c \left(\frac{R_C}{L_\rho}, -\gamma \right) - f_c \left(\frac{R_I}{L_\rho}, -\gamma \right)} \right], \quad (B12)$$

1267 The effective temperature associated with dissipation from secular cooling is
 1268 almost identical to T_D but slightly hotter:

$$1269 \quad T_S = \frac{T(R_I)}{\left[1 - \left(\frac{R_I}{L_\rho}\right)^2 - A_\rho \left(\frac{R_I}{L_\rho}\right)^4\right]^\gamma} \frac{\left[f_c\left(\frac{R_C}{L_\rho}, \gamma\right) - f_c\left(\frac{R_I}{L_\rho}, \gamma\right)\right]}{\left[f_c\left(\frac{R_C}{L_\rho}, 0\right) - f_c\left(\frac{R_I}{L_\rho}, 0\right)\right]}. \quad (B13)$$

1270 Finally, we can calculate the dissipation sink associated with the thermal
 1271 conductivity of the core fluid:

$$1272 \quad \Phi_K = 16\pi\gamma^2 k_C L_\rho \left[f_k\left(\frac{R_C}{L_\rho}\right) - f_k\left(\frac{R_I}{L_\rho}\right) \right] T_D, \quad (B14)$$

1273 where our last useful function is

$$1274 \quad f_k(x) = 0.2x^5 \left[1 + \frac{10}{7}(1 + 2A_\rho)x^2 + \frac{5}{9}(3 + 10A_\rho + 4A_\rho^2)x^4 \right]. \quad (B15)$$

1275 Note that we can then write the total adiabatic heat flow in terms of Φ_K :

$$1276 \quad Q_{AD} = \left(\frac{T_S T_{CMB}}{T_D (T_S - T_{CMB})} \right) \Phi_K \quad (B16)$$

1277 which is an energy-based definition that is basically equivalent to the usual
 1278 formula, $Q_{AD} \sim 4\pi R_C^2 k_C (dT_a/dr)$, derived from Fourier's law.

1279

1280 APPENDIX C. MAGNETIC DIFFUSION TIME

1281 We determine the time it takes for the field to decay after convection
 1282 ceases following the procedure detailed in Stevenson (2003) to approximate
 1283 the magnetic diffusion time:

$$1284 \quad \tau = \frac{R_C^2}{\pi^2 \lambda}. \quad (C1)$$

1285 Here R_C is radius of the electrically conducting region (i.e., the core) and λ
 1286 is magnetic diffusivity given by:

$$1287 \quad \lambda = \frac{1}{\mu_0 \sigma}, \quad (C2)$$

1288 where μ_0 is the permeability of free space and σ is the electrical
 1289 conductivity. We assume $\lambda \sim 1 \text{ m}^2/\text{s}$, appropriate for terrestrial planets with a
 1290 liquid iron alloy core (e.g., Schubert and Soderlund 2011), such that the
 1291 magnetic field will diffuse across the core in $\tau \sim 400$ years.

1292

1293 APPENDIX D: TABLES

1294

Table D1
Description of Model Constants

Term	Description	Value
μ_0	Permeability of free space	$1.257 \times 10^{-6} \text{ H}\cdot\text{m}^{-1}$
G	Gravitational constant	$6.67 \times 10^{-11} \text{ m}^3\cdot\text{kg}^{-1}\cdot\text{s}^{-2}$
R	Universal gas constant	$8.3145 \text{ J}\cdot\text{K}^{-1}\cdot\text{mol}^{-1}$
R_M	Radius of the Moon	1737 km
R_c	Radius of the core	350 km
Ω	Angular velocity of the Moon	$2.66 \times 10^{-6} \text{ rad}\cdot\text{s}^{-1}$
K_0	Effective modulus	$121.4 \times 10^9 \text{ Pa}$
K_1	Effective derivative of effective modulus	5.7871
A_p	Constant in density profile	1.59
ρ_0	Central density	$6477 \text{ kg}\cdot\text{m}^{-3}$
P_0	Central pressure	$5.15 \times 10^9 \text{ Pa}$
M_c	Mass of the core	$1.16 \times 10^{21} \text{ kg}$
V_c	Volume of the core	$3.95 \times 10^{16} \text{ m}^3$
g	Gravitational acceleration near the core-mantle boundary	$0.6311 \text{ m}\cdot\text{s}^{-2}$
γ	Grüneisen parameter for the core	1.65
C_c	Specific heat of the core	$835 \text{ J}\cdot\text{kg}^{-1}\cdot\text{K}^{-1}$
ΔS_c	Entropy of melting for the inner core	$200 \text{ J}\cdot\text{K}^{-1}\cdot\text{kg}^{-1}$
α_I	Coefficient of compositional expansion for enriching the outer core in sulfur	2.3
λ_K	Average decay constant for potassium-40	$1.76 \times 10^{-17} \text{ s}^{-1}$
H_K	Heat production rate for potassium-40	$4.2 \times 10^{-14} \text{ W}\cdot\text{kg}^{-1}\cdot\text{ppm}^{-1}$
c	Constant of proportionality in equations 5–7	0.63
dT_L/dc	Compositional dependence of liquidus temperature	-2500 K
dT_L/dP	Pressure dependence of liquidus temperature	$3 \times 10^{-8} \text{ K}\cdot\text{Pa}^{-1}$

1296

1297

1298

1299

Table D2		
Definition of Model Inputs and Outputs		
Variable	Definition	Values
Input parameters		
[S]	Abundance of sulfur in the core ^a	1–6 wt%
[K]	Abundance of potassium in the core ^b	0–50 ppm
k_c	Thermal conductivity of the core ^c	10–50 $\text{W m}^{-1} \text{K}^{-1}$
Q_c	Present-day heat flow across the core-mantle boundary ^d	0–2 GW
Energy budget outputs of the core		
Q_{CMB}	Heat flow across the core-mantle boundary	GW
Q_L	Latent heat from inner core nucleation	GW
Q_G	Gravitational energy released from inner core nucleation	GW
Q_R	Radiogenic heating in the core	GW
Q_S	Secular cooling of the core	GW
Entropy budget outputs of the core		
Φ_{CMB}	Dissipation available to power a dynamo	MW
Φ_L	Dissipation associated with latent heat	MW
Φ_G	Dissipation associated with gravitational energy	MW
Φ_R	Dissipation associated with radiogenic heating	MW
Φ_S	Dissipation associated with secular cooling	MW
Φ_K	Dissipation sink associated with thermal conductivity	MW

1300 ^aWeber et al. 2011.

1301 ^bLaneuville et al. 2014, Scheinberg et al. 2015, Hirose et al. 2013.

1302 ^cPommier 2018.

1303 ^dLaneuville et al. 2014.